Transit-time and temperature control the spatial patterns of aerobic respiration and denitrification in the riparian zone

G. E. H. Nogueira[1]*, C. Schmidt[1,2], P. Brunner[3], D. Graeber[2], J. H. Fleckenstein[1,4]

[1] Department of Hydrogeology, Helmholtz-Centre for Environmental Research - UFZ, Leipzig, Germany.

[2] Department of Aquatic Ecosystem Analysis, Helmholtz-Centre for Environmental Research - UFZ, Magdeburg, Germany.

[3] Centre for Hydrogeology and Geothermics, University of Neuchâtel, Neuchâtel, Switzerland.

[4] Bayreuth Centre of Ecology and Environmental Research, University of Bayreuth, Bayreuth, Germany

* corresponding author: Guilherme E. H. Nogueira (guilherme.nogueira@ufz.de)

Key Points

Fully-integrated 3D transient flow model coupled to a temperature-dependent flow path-reaction model to assess riparian solutes turnover

Turnover mainly controlled by high temperature in summer; in winter solute concentrations and transit-times variations become more important

Assessments of riparian turnover restricted to near stream areas might overlook processes affecting overall downstream water quality

This article has been accepted for publication and undergone full peer review but has not been through the copyediting, typesetting, pagination and proofreading process, which may lead to differences between this version and the Version of Record. Please cite this article as doi: 10.1029/2021WR030117.

Abstract

During the flow of stream water from losing reaches through aquifer sediments, aerobic and anaerobic respiration (denitrification) can deplete dissolved oxygen and nitrate (NO_3^-), impacting water quality in the floodplain and downstream gaining reaches. Such processes, which vary in time with short and long-term changes in stream flow and temperature, need to be assessed at the stream corridor scale to fully capture their effects on net turnover, but this has rarely been done. To address this gap, we combine a fully-integrated 3D transient numerical flow model with temperature-dependent reactive transport along advective subsurface flow paths to assess aerobic and anaerobic respiration dynamics at the stream corridor scale in a predominantly losing stream. Our results suggest that given carbon availability (as an electron donor), complete NO_3^- removal occurred further away from the stream after complete oxygen depletion and was relatively insensitive to variations in temperature and transit-times. Conversely, transit-times and oxygen concentrations constrained nitrate removal along short hyporheic flow paths. Even under limited carbon availability and low-temperatures, NO_3^- removal fractions (R_{NO3}) will be greater at locations further from the stream than along shorter hyporheic flow paths (R_{NO3}=0.4 and R_{NO3}=0.1, respectively). With increasing temperature, the relative effects of stream flow and solute concentrations on biogeochemical turnover and the redox zonation around the stream decreased. The study highlights the importance of seasonal variations of stream flow and temperature for water quality at the stream-corridor scale. It also provides an adaptive framework to assess and quantify reach-scale biogeochemical turnover around dynamic streams.

Keywords: biogeochemical turnover, temperature, denitrification, floodplain, hydrogeosphere, transient simulation

1. Introduction

The exchange zone between streams and their surrounding riparian groundwater is essential for solute turnover and the ecological regulation of stream ecosystems (Bernhardt et al., 2017; Mayer et al., 2006; Vidon & Hill, 2006). In this zone, water and solute exchange strongly vary in time and space, being influenced by different factors, such as stream stage, aquifer properties, and hydraulic connectivity (Kurz et al., 2017; Munz et al., 2017; Ocampo et al., 2006; Oldham et al., 2013), leading to significant changes in water quality. Both short-term and seasonal stream stage fluctuations modify water and solute exchange fluxes and affect short- and long term biogeochemical responses in the riparian zone (Boutt & Fleming, 2009; Chen et al., 2020; Diem et al., 2013; Jensen et al., 2017; Liang et al., 2018; Liao et al., 2014; Liu et al., 2019; Sawyer et al., 2014).

Several studies have illustrated the importance of aerobic respiration (AR) and the resulting dissolved oxygen (DO) depletion in regulating the redox conditions of near stream environments, affecting the turnover of redox-sensitive compounds like nitrate (NO_3^-) via denitrification (DN) (Boano et al., 2010; Briggs et al., 2015; Frei et al., 2012; Rivett et al., 2008; Sharma et al., 2012; Shuai et al., 2017; Trauth et al., 2014; Zarnetske et al., 2011). DO consumption and the subsequent redox reactions are jointly governed by hydrologic dynamics (e.g., changes in water transit-times) and the reaction rates that are temperature dependent, both of which are subject to short-term (event scale) and long-term (seasonal scale) fluctuations. A rising stream stage will increase the hydraulic gradients between the stream and local groundwater (GW), increasing stream water (SW) infiltration fluxes and reducing the transit-times of infiltrating water parcels. Additionally, short-term and seasonal temperature variations affect biogeochemical reaction rates, leading to different chemical patterns depending on the combination of transport and reaction processes at a given time and location (Nogueira et al., 2021; Song et al., 2018; Vieweg et al., 2016), which are often not explicitly considered in studies on SW-GW interactions.

In predominantly losing stream reaches, which are becoming increasingly common as a result of global change (Jasechko et al., 2021), and not just in semi-arid and arid regions, the exchange zone expands beyond the streambed and hyporheic zone into the floodplain (Brunner et al., 2009; Irvine et al., 2012; Treese et al., 2009). For these conditions, it is not sufficient to only look at the streambed and banks, and instead, an evaluation of the entire stream corridor and its complex 3D geometry is needed for an adequate assessment of DO dynamics and the resulting turnover potentials, e.g. for NO_3^-, at the system-scale. As high-resolution monitoring campaigns are hard to implement at the scale of entire stream corridors, numerical models are good tools to achieve such understanding (Brunner et al., 2017).

Most modelling studies to date, however, have either looked at idealised 2D systems primarily focusing on the streambed and stream banks or have focused on individual aspects, such as temperature effects on turnover or effects of short-term dynamics (e.g., discharge events) and not jointly at event- and seasonal times scales. For instance, Zheng et al. (2016) used an idealised 2D model to illustrate the effects of temperature variations on DN below a bed form-induced hyporheic zone using steady-state flow fields. Trauth and Fleckenstein (2017) used a 3D coupled flow and reactive transport numerical model to assess impacts of discharge events on hyporheic turnover assuming constant water temperature, revealing how short-term events increased the hyporheic reactive efficiency (solute consumption as a fraction of influx) of an in-stream gravel bar. While Song et al. (2018) jointly assessed the impacts of high-frequency stream stage and thermal variations on biogeochemical reactions in the hyporheic zone, their 2D model was spatially limited to the stream banks, disregarding turnover processes in the floodplain. These and other recent studies (Shuai et al., 2017; Singh et al., 2020) have illustrated the effects of hydrologic conditions and landscape controls on water flux and reactive solute transport in streambeds and banks. To our knowledge, the combined effects of flow (transit-times) and temperature on riparian DO concentrations and subsequent DN across event and seasonal time scales have not yet been fully addressed in an integrated modelling study of an entire stream corridor.

This study aims to overcome some of these deficiencies by jointly assessing the hydraulic (flow variations, transit times) and thermal controls (temperature) of the biogeochemical reactions of DO and DN in a riparian aquifer that receives DO-rich SW infiltration from a predominantly losing stream reach. We employ an adaptive method to couple biogeochemical processes to a fully-coupled and spatially-distributed numerical flow model based on a particle tracking analysis using a Lagrangian flow path-reaction approach to evaluate DO and nitrate turnover at the stream corridor scale, using a simplified representation of key reactions along subsurface flow paths. With that, we address the following three major research questions: (1) How do variable hydrological and biogeochemical conditions affect the biogeochemical turnover of stream borne DO and NO_3^- in the riparian aquifer? (2) How do stream flow and water temperature variations shape the aerobic zone (DO_z) around the stream? and (3) How do riparian DO dynamics affect DN patterns of NO_3^- in the riparian corridor for different transient streamflow and temperature scenarios? We conducted an explorative modelling informed by data from the well-instrumented Selke site as a test-case to address these questions. Combining advective particle tracking with the simulation of biogeochemical reactions along the identified flow paths using field temperature and solute concentration data to constrain the model, we assess the impacts of stream flow and temperature variations on patterns of DO and NO_3^- concentrations in the riparian aquifer.

2. Materials and Methods

In this section, following the study site presentation, we describe how we developed and calibrated the numerical flow model. We then present how we implemented the reactive transport of specific solutes (coupling hydrology and biogeochemistry). We also describe how we evaluated the results and which scenarios we considered for analyses.

2.1. Field Site and data collection

The study site is located within the Selke River catchment, a 4th-order perennial stream (low discharge=0.23 m^3s^{-1}, mean discharge=1.51 m^3s^{-1}, and high discharge=15.6 m^3s^{-1}), central Germany, around the high-intensity test-site of a TERENO observatory (Wollschläger et al., 2017). The studied stream reach (appx. 900 m) is characterised by net losing conditions, with downstream discharge generally 25% smaller than discharge upstream (Schmadel et al., 2016). The local aquifer consists of up to 8 m-thick fluvial sediments, with grain sizes ranging from medium sands to coarse gravels, underlain by less permeable clay-silt deposits forming the bottom of the alluvial aquifer.

Hydraulic heads and stream stage were continuously measured for a period of one year (2017-2018) with a temporal resolution of 10 min. The hydraulic heads were measured in 20 piezometers distributed in the area. Head measurements in nested piezometers varied equally for shallow and deep wells (Nixdorf & Trauth, 2018). Stream stage values were converted to stream discharge (Q), available through a stream stage-discharge relationship based on biweekly manual discharge measurements. Also, a total of seven high-resolution well-to-well tracer-tests were carried out near the stream covering a whole hydrological year (2017-2018) and providing extra information about flow dynamics and main groundwater flow directions. Detailed descriptions of these experiments can be found in Nogueira et al. (2021). DO concentrations were monitored by self-contained loggers (HOBO Dissolved Oxygen Data Logger) in both stream and in groundwater with a 10-min interval. Further hydrochemical data (such as DOC and NO_3^- concentrations) was assessed through manual sampling in a biweekly interval, which were analysed in the laboratory following standard procedures for stream water and groundwater sampling and analyses as described in Trauth et al. (2018).

2.2. Integrated surface-subsurface flow and mass transport

The fully integrated surface-subsurface flow and transport model HydroGeoSphere (*https://www.aquanty.com/hydrogeosphere*) was used to simulate water and solute exchange across the SW-GW continuum. HydroGeoSphere (HGS) is a finite element code that solves Richards' equation for variably saturated flow in three-dimensions (Brunner & Simmons, 2012; Simmons et al., 2020). Overland flow is solved numerically using the diffusion-wave equation together with Manning's equation. For coupling the surface and groundwater environments, we selected the dual node approach to approximate the continuity of pressure heads. The approach assumes that exchange fluxes among the domains depend on the hydraulic head gradient across a coupling interface, the vertical saturated hydraulic conductivity, and a coupling length value (Therrien et al., 2010). The coupling length represents the thickness of the interface between the two domains, which enforces near-continuity between the surface and subsurface, minimising the influence of the first-order coupling coefficient while preserving the underlying physics-based nature of the model (Ebel et al., 2009). Details on the governing flow and transport equations for HGS can be found in Therrien et al. (2010).

2.2.1. Flow and mass transport model setup

The extent of the model domain is approximately 900 m x 770 m x 10 m (width, length, and thickness, Figure 1). An unstructured 2D triangular mesh of finite elements was generated with the Algomesh software (2018 HydroAlgorithmics Pty Ltd) for the top of the domain, representing the land and streambed surfaces. The topography of the domain was interpolated from an aerial survey covering the floodplain and the streambed, with a horizontal resolution of 1 m and a vertical accuracy of 0.1 m. The triangular element sizes varied from a maximum of up to 40 m in the floodplain to about 2.0 m in the streambed and were further refined to about 1.0 m around observation wells in the near-stream riparian zone (FS wells, Figure 1). The 2D mesh is replicated in the vertical direction to form a 3D mesh consisting of quadrilateral elements in 15 layers, with thicknesses varying from 0.1 m in the top layers to 2.0 m in the bottom layer of the model (~152 masl). The depth of the lower boundary of the domain was set according to the less permeable clay-silt deposits that form the bottom of the alluvial aquifer (around 7-8 m below the surface). A total of 136,682 elements and 74,955 nodes comprise the model domain.

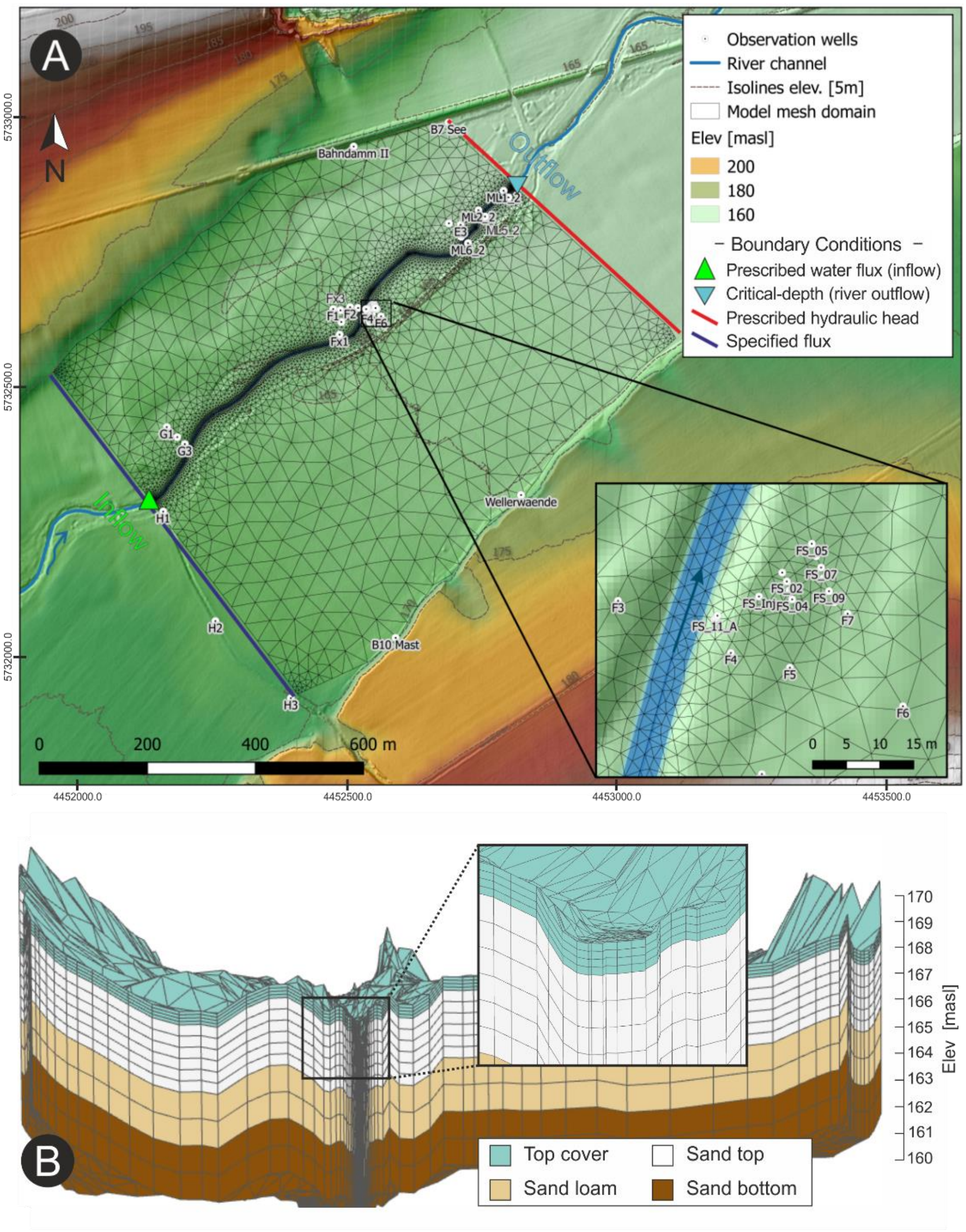

Figure 1: a) Mesh of the model domain and applied BC's; the inset plot shows the region where well-to-well tracer-tests were performed; **b)** lateral view of model domain coloured with hydrogeological units, and detail to layer thickness on the top cells near the stream.

We divided the aquifer into four units with anisotropic hydraulic conductivity (initial Kx=Ky and Kxy/Kz=10, Table 1) based on field data and previously conducted geological surveys of the area (Figure S1, supplementary material). Van Genuchten parameters (Genuchten, 1980) were assigned based on literature values typical for medium sand. For the two bottom units, these values are merely a characteristic of the material as they remain fully-saturated throughout the year. We defined two different set of surface properties (Manning's roughness coefficients, *x* and *y* friction values, and rill storage heights) for the streambed and floodplain. In contrast, different coupling lengths were assigned for individual reaches of the streambed, and another for the floodplain areas. This guarantees a more flexible parameterisation in terms of exchange fluxes between SW-GW for the different stream reaches and the floodplain during model calibration.

Table 1 – *Flow and transport parameters for HGS model*

Parameter	Symbol	Initial values	Final values (calibrated)
Surface (streambed / floodplain)			
Friction streambed (roughness, x=y) (m s$^{-1/3}$)[a]	F_r	0.04	--
Friction floodplain (roughness, x=y) (m s$^{-1/3}$)[a]	F_f	0.30	--
Coupling length stream (range) (m)	l_s	0.1-10	0.1-15
Coupling length floodplain (m)	l_e	0.1	8
Rill storage height (both areas) (m)[a]	r	1.0x10^{-4}	--
Porous media (for each zone/material)			
Top cover – Porosity ([-])	n	0.2	0.29
Hydraulic conductivity (m s^{-1})	K_x; K_y; K_z	1.0x10^{-3}; 1.0x10^{-3}; 1.0x10^{-4}	7.9x10^{-4}; 1.5x10^{-3}; 4.3x10^{-4}
Long; Trans; Vert. Dispersivity (m)	α_L; α_T; α_V	1.0; 1.0; 1.0	8.3; 1.2; 0.08
Residual saturation; *α; ß* ([-]; m^{-1};[-])[a]	θ_s; α; β	0.1; 8.0; 2.0	--
Sand top – Porosity ([-])	n	0.2	0.28
Hydraulic conductivity (m s^{-1})	K_x; K_y; K_z	1.0x 10^{-3}; 1.0x10^{-3}; 1.0x10^{-4}	7.5x10^{-3}; 6.5x10^{-3}; 2.2x10^{-4}
Long; Trans; Vert. Dispersivity (m)	α_L; α_T; α_V	1.0; 1.0; 1.0	0.6; 0.26; 0.15
Residual saturation; *α; ß* ([-]; m^{-1};[-])[a]	θ_s; α; β	0.045;14.0; 2.0	--
Sandy loam – Porosity ([-])	n	0.2	0.26
Hydraulic conductivity (m s^{-1})	K_x; K_y; K_z	7.0x10^{-4}; 7.0x10^{-4}; 7.0x10^{-5}	7.2x10^{-3}; 6.0x10^{-4}; 4.9x10^{-5}
Long; Trans; Vert. Dispersivity (m)	α_L; α_T; α_V	1.0; 1.0; 1.0	1.2; 1.5; 0.18
Residual saturation; *α; ß* ([-]; m^{-1};[-])[a]	θ_s; α; β	0.06; 14.0; 2.0	--
Sand bottom – Porosity ([-])	n	0.2	0.31

Hydraulic conductivity (m s^{-1})	K_x; K_y; K_z	$1.0\text{x}10^{-3}$; $1.0\text{x}10^{-3}$; $1.0\text{x}10^{-4}$	$1.1\text{x}10^{-2}$; $3.5\text{x}10^{-3}$; $3.3\ \text{x}10^{-4}$
Long; Trans; Vert. Dispersivity (m)	α_L; α_T; α_V	1.0; 1.0; 1.0	1.0; 0.98; 0.07
Residual saturation; *α; ß* ([-]; m^{-1};[-])[a]	θ_s; *α; ß*	0.045; 14.0; 2.0	--

a = not included in the calibration

Initial conditions for the hydraulic heads for the whole domain were achieved by a first model run (appx. one year in simulation time) using constant, average values for hydraulic heads, precipitation and stream discharge (i.e., *quasi-steady state* conditions). Next, a transient run with daily updated boundary conditions (BCs) from Nov 2016 to Nov 2017 (i.e., *spin-up period*) was performed to achieve realistic hydraulic heads throughout the domain. Following the *spin-up period*, the model was run with a similar time-step updating of the BCs, when automated calibration and model validation were carried out based on observed GW heads, stream discharge, and tracer breakthrough curves (BTCs) as described in the model calibration section below (see also Figure S2, supplementary material). For this last period, two other BCs were implemented to represent the performed tracer-tests. The following BCs were applied in the model:

- Prescribed hydraulic head (Dirichlet) applied at the northern side of the model domain representing hydraulic heads at the downstream side of the study area. Based on measured hydraulic heads in the wider area of the floodplain (observation wells outside the study site), the heads were linearly interpolated and extended to the entire domain lateral. The heads were updated according to observed field values, representing the GW seasonal fluctuations.
- Prescribed water flux (Neumann) applied at the Southside (upstream) of the model domain representing GW inflow. A constant GW flow boundary was selected instead of prescribed hydraulic heads because early model runs showed that this option resulted in a better representation of water table fluctuations near the boundary. An initial value of 2.5 m^3d^{-1} was chosen based on the outflow from the *quasi-steady state* model run. A constant optimised value of 2.6 m^3d^{-1} was found through automated calibration.
- No flow boundary applied at the East and West sides, as well as on the bottom of the model domain.
- Prescribed water flux (Neumann) applied at the stream inlet (at a daily time resolution), according to discharge measurements at the nearby gauging station at Meisdorf (51°41’29.1’’N, 11°17’02.2’’E).
- Critical-depth boundary applied at the stream outlet, forcing the water depth at the boundary to be equal to the critical depth, which is calculated by the model together with stream discharge.

- Groundwater recharge applied at the surface of the domain. Daily precipitation was measured at the nearby climate station Aschersleben (51°43’33.6’’N, 11°30’39.6’’E) of the German weather service. Evapotranspiration (ET) rates were computed through HYDRUS-1D and used to calculate the percentage from rainfall applied in the model surface as GW recharge. No further internal calculations of ET were done in the model. For the simulation period, recharge values varied over time, ranging from 28% to 36% of total precipitation (mean= 33%, std.d= 4.8%). However, since deviations from the mean value were not large, a constant value of 33% of observed daily precipitation value was applied as GW recharge in each time-step.
- For the tracer tests, the additional BC were implemented accordingly: 1) Prescribed water flux (Neumann) describing the injected water volume for the injection periods. 2) Specified mass flux representing the total added tracer mass. This guarantees correct representation of both flow and mass changes in the system (Table S1, supplementary material). Both BCs were applied to a single subsurface node 2.5 m below the surface at FS-inj (Figure 1) representing the nearest depth in which tracer was injected.

2.2.2. Flow and mass transport calibration and evaluation

The model was calibrated against the observed GW heads and stream discharge (covering 130 days of high-frequency measurements), as well as measured tracer concentrations from 8 of the 18 BTCs recorded in different aquifer depths during tracer-tests (Nogueira et al., 2021). Hydraulic and transport parameters were calibrated simultaneously against all available observation types using a weighted multivariate objective function through PEST (J Doherty, 1994, 2018). A simultaneous calibration of all model parameters against all observation types has the potential to provide a better model parametrisation as discussed in detail in Doherty (2003), Moore et al. (2010), and Schilling et al. (2019). We utilised a Tikhonov regularisation to address parameter nonuniqueness, introducing a penalty to the objective function if parameters under calibration diverge excessively from preferred values (prior knowledge of field parameters). Different observation types were weighted to feature equally in the objective function by using the PEST software suite PWTADJ1 (J. E. Doherty & Hunt, 2010), and tracer concentrations were inversely weighted to give higher importance to the tails of BTCs.

We evaluated the model quality using the average water balance error, the mean absolute error (MAE) between observed and simulated heads and tracer concentrations, as well as the Nash Sutcliffe efficiency (NSE) criteria. Model results were visualised with ParaView, Version 5.8.1 (Ahrens et al., 2005), and with TecPlot 360 EX, Version 2019 R1 (Constellation Software, Inc.).

2.2.3. *Flow paths and particle tracking analysis*

To evaluate the effects of stream stage changes on groundwater transit-times, and subsurface biogeochemical processes in infiltrating SW, we used the transient velocity fields from HGS for an advective particle tracking analysis. Particle transport is based on a second-order Runge-Kutta integration of simulated subsurface velocity fields using the software TecPlot 360 EX. Massless particles were released from each mesh cell at the wetted streambed in every time-step (around 1,800 particles per time-step), being subjected to subsequent changes of the velocity fields until the end of the simulation or until they have left the model domain (either back to the stream or via the subsurface boundary). A continuous release of particles in each time-step assures that they are subjected to transitions in GW velocity fields that are influenced by stream stage variations. The locations, transit-times and velocities of each particle were then extracted in each time-step for the following flow path-reaction simulations.

2.3. *Flow path reactive transport: coupling hydrology and biogeochemistry*

2.3.1. *Coupled reactions and reaction rate calculations*

Since in HGS it is not yet possible to simulate temperature-dependent reactions, we employed a Lagrangian flow path-reaction model based on the particle tracking results. A similar biogeochemical simulation along individual subsurface flow paths was employed by Frei et al. (2012). Reactions occur in individual sub-sections (i) of each flow path, based on the extracted particle transit-times and locations. The integration time-step between flow path sub-sections was on average 0.1 day (±0.9 day) with larger intervals only towards the end of each flow path, guaranteeing a good spatio-temporal discretisation of the transport problem. We implemented the respective reaction equations in MATLAB® (Figure S3, supplementary material). We focused on the simulation of redox-sensitive biogeochemical processes in the riparian zone, specifically aerobic respiration (AR) and denitrification (DN) of organic matter (DOC) represented by carbohydrate CH_2O, according to the following reaction equations:

$$\text{Aerobic respiration: } CH_2O + O_2 \rightarrow CO_2 + H_2O \tag{1}$$

$$\text{Denitrification: } 5CH_2O + 4NO_3^- + 4H^+ \rightarrow 5CO_2 + 2N_2 + 7H_2O \tag{2}$$

We did not incorporate nitrification into our simulations, specifically the production of nitrate (NO_3^-) from oxidation of Ammonium (NH_4^+), since observed NH_4^+ concentrations are very low at the site (<0.1 mg L^{-1} in stream water and in groundwater) in comparison to NO_3^- concentrations (Trauth et al., 2018). As shown by Zheng et al. (2016), high values of $\log_{10}([NO_3^-]/[NH_4^+])$ ratios (such as 1.3 in stream water at the studied site) would lead to a NO_3^- net removal higher than production; thus we consider nitrification to be negligible in the simulations. Based on Eq.(1) and Eq.(2), a DOC source can react with dissolved oxygen (DO) and NO_3^-. We assumed that solute transport into the subsurface was purely driven by infiltrating stream water, and that reaction rate coefficients are temperature-dependent. Apart from the first sub-section of each flow path, solute concentrations and reaction rates for a subsequent sub-section are based on results of the preceding sub-section (Figure S3, supplementary material). Reactions were simulated using Monod-kinetics with an inhibition coefficient (K_I) for DN, hence, significant NO_3^- consumption occurs only if DO concentrations are below 1.0 mgL^{-1} (K_I=0.031 mmolL^{-1}) (Widdowson et al., 1988; Zarnetske et al., 2011). With this formulation, denitrification can still occur (however at much lower rates) even if bulk DO concentrations indicate aerobic conditions. Completely disregarding denitrification under aerobic conditions would be an oversimplified assumption, since it can still take place within redox microzones of oxic-saturated sediments (e.g., Briggs et al., 2015; Song et al., 2018). Furthermore, we only analysed fully-saturated flow paths. In this way, we do not have to account for re-oxygenation that could affect the biogeochemical processes (Frei et al., 2012). Moreover, all DOC is assumed to be bioavailable and can be consumed for both AR and DN until its exhaustion following the reaction rate coefficients in each sub-section:

$$k_{AR(t)} = f_T\left[\mu_{max\_AR}\left(\frac{C_{DO(t)}}{K_{DO}+C_{DO(t)}}\right)\left(\frac{C_{DOC(t)}}{K_{DOC}+C_{DOC(t)}}\right)\right] \tag{3}$$

$$k_{DN(t)} = f_T\left[\mu_{max\_DN}\left(\frac{C_{NO3(t)}}{K_{NO3}+C_{NO3(t)}}\right)\left(\frac{C_{DOC(t)}}{K_{DOC}+C_{DOC(t)}}\right)K_I\right] \tag{4}$$

where k_{AR} and k_{DN} are the actual reaction rates of DO and NO_3^-, respectively; μmax_{AR} and μmax_{DN} represent maximum reaction rates for AR and DN, respectively; C_{DO}, C_{DOC} and C_{NO3} are the concentrations of DO, DOC and NO_3^-; and K_{DO}, K_{DOC} and K_{NO3} are the half-saturation constants for DO, DOC and NO_3^-, respectively, Table 2. The maximum reaction rate of AR (μmax_{AR} = 0.478 mmol $L^{-1}d^{-1}$ = 15.3 mg $L^{-1}d^{-1}$) was based on field values (Trauth et al., 2014), while maximum reaction rate of DN (μmax_{DN} = 0.086 mmol $L^{-1}d^{-1}$ = 5.3 mg $L^{-1}d^{-1}$), as well the solute half-saturation constants were based on values from the literature (Gu et al., 2007; Trauth et al., 2014; Zarnetske et al., 2011). To account for the temperature dependency of rate coefficients, the temperature factor (f_T) is introduced in Eq.(3) and Eq.(4) according to the expression proposed by O'Connell (1990):

$$f_{T(t)} = exp\left[a + \ b\ T_{GW(t)}\left(1 - 0.5\ \frac{T_{GW(t)}}{T_{opt}}\right)\right] \tag{5}$$

where a and b are fitting parameters, T_{GW} is the groundwater temperature, and T_{opt} is the optimal temperature for DOC consumption taken as 35°C (Diem et al., 2013; Greskowiak et al., 2006; Kirschbaum, 1995; Sharma et al., 2012). Different from the commonly used Arrhenius equation, we selected this form of rate dependency because it better follows the concept that bulk microbial biomass, and the availability of substrates decrease with increasing temperature and thus, reaction rates tend to decline when temperatures are above an optimal value for microbial activities(Čapek et al., 2019; Carey et al., 2016; PeterJohn, 1991; Pietikäinen et al., 2005; Schipper et al., 2014). We parameterised f_T using combined in-situ measurements of DO and electrical conductivity (EC) from carried out tracer-tests. In-situ apparent AR rate coefficients were computed based on EC transit-times and related to T_{GW} at the time of the experiment (Figure S4, Supplementary material). The same temperature factor was used to compute the actual DN rates (k_{DN}) since it is expected that denitrification follows the same pattern of increasing rates with temperature up to 35-40°C (Boulêtreau et al., 2012; Veraart et al., 2011), whereas rates tend to rapidly decline when temperatures are above this threshold and approach zero when temperature is above 60 °C (PeterJohn, 1991). The a and b estimations (-3.5 and 0.22, respectively) were within the range of literature values, and have been successfully applied in other river bank filtration studies that simulate DO and NO_3^- reactions (Diem et al., 2013; Greskowiak et al., 2006; Henzler et al., 2016; Kirschbaum, 2000; Sharma et al., 2012). Final computed actual AR and DN rates were within the range of literature values (Maag et al., 1997; Matsunaga et al., 1993; Precht et al., 2004) (Figure S4 and Table S2, supplementary material).

Infiltrating SW with a different temperature than that of GW impacts the reaction rate coefficients in the vicinity of the stream (Nogueira et al., 2021; Song et al., 2018). However, short-term temperature variations induced by infiltrating stream water are strongly damped within a few decimetres (e.g. Engelhardt et al., 2013) and we expect that flow path temperatures (i.e., temperature of water along infiltrating flow path) reach T_{GW} after relatively short transit-times (Munz et al., 2017; Rau et al., 2014; Vieweg et al., 2016), especially further away from the stream (Trauth et al., 2018). For the spatial scale of our analysis (tens to hundreds of meters) temperature variations occur predominantly at seasonal time scale. Therefore, to represent the expected water temperature at the floodplain, monthly averaged T_{GW}

from piezometers that are also affected by infiltrating stream water to a certain extent were used in Eq.(5), which lies between stream water temperature (strongly varying over the year, 8.5°C±6.0) and the temperature of the end-member groundwater far from the stream (solely influenced by seasonality, 10°C±1.5) (Figure S5, supplementary material). By using monthly averaged groundwater temperatures, the seasonal subsurface temperature variations were well captured. With this approach, simulations of DO concentrations using transit-times derived from the HGS model yielded a NSE=0.82 and R^2=0.91 for a near stream well during the same observation period (Figure S5, supplementary material).

2.3.2. Initial solute concentrations for flow path reactions

Solute concentrations and reaction rates for the first sub-section (i) of each flow path were based on initial solute concentrations (Table 2). There was no other groundwater-borne solute contribution within flow paths; solute transport into the subsurface was purely driven by infiltrating stream water. Locally, SW is saturated in DO prior to infiltration, therefore we assigned a constant initial DO concentration of 0.31 $mmolL^{-1}$ (10 mgL^{-1}) for the first sub-sections of the flow paths. Time series of DOC at a stream gauging station 5 km upstream of the site showed varying concentrations between 10 and 30 mgL^{-1} (Trauth et al., 2014). In the simulations, however, we assumed a constant DOC concentration of 0.66 mmol L^{-1} (20 mgL^{-1}), almost twice the molar mass of DO, to ensure that there is a DOC source available for denitrification after near-complete DO depletion.

For initial NO_3^-, in a first scenario, concentrations were related to stream discharge to represent the patterns of increase in solute concentrations with rising discharge (Dupas et al., 2017; Musolff et al., 2015; Sawyer et al., 2014; Trauth & Fleckenstein, 2017). At our site, field data indicates a nearly linear increase of NO_3^- concentration with discharge (Figure S6, supplementary material). Simulated NO_3^- concentrations using this relation matched well observed NO_3^- concentrations in a groundwater well (NSE=0.53 and R^2=0.75, Figure S6, supplementary material). To further assess the reactive potential of denitrification of the floodplain for elevated NO_3^- concentrations (e.g., coming from soil top or from larger distance groundwater), we ran additional scenarios considering a high constant initial value of 1.0 $mmolL^{-1}$ (62 mgL^{-1}) for NO_3^- concentrations, which also reflects the high NO_3^- concentrations at the groundwater on the site (Trauth et al., 2018). Although mean stream-borne NO_3^- is much lower than groundwater-borne NO_3^-, by imposing the high initial concentrations we can assess where significant NO_3^- turnover occurs regardless of the origin of the source, thus estimating the overall locations of high DN rates within the floodplain. The constant initial solute concentrations may be considered unrealistic regarding the usual relationship between solute concentrations and discharge for most streams, but by doing this the effects of pure changes in hydraulic and thermal conditions can be better evaluated in these scenarios.

Table 2 – *Parameter values used in defining the reaction kinetics.* †

Rate constants (Eq.3 and Eq.4)	*Value*
μmax_{AR}	0.4780 mmol $L^{-1}d^{-1}$
μmax_{DN}	0.0864 mmol $L^{-1}d^{-1}$
Half saturation constants (Eq.3 and Eq.4)	
K_{DO}	0.00625 mmol L^{-1}
K_{DOC}	0.10700 mmol L^{-1}
K_{NO3}	0.03230 mmol L^{-1}
Inhibition coefficient for Denitrification (Eq.4)	
I_{DO}	0.03130 mmol L^{-1}
Temperature factor (f_T) (Eq.3 and Eq.4)	
a	-3.5
b	0.22
T_{opt}	35°C

Initial solutes concentrations for each flow path

Solute	*Initial concentration in mmol L^{-1} (mg L^{-1})*
Dissolved Oxygen (DO)	0.31 (*10.0*)
Organic Matter (DOC)	0.66 (*20.0*)
Nitrate (NO_3^-)	0.08xQ+0.048 (*5xQ+3*)
Nitrate (NO_3^-) – additional scenarios	1.00 (*62.0*)

† *The values in round brackets are the concentrations in mg L^{-1}; Q is the stream discharge.*

To assess the interplay between transit-times and water temperature on the biogeochemical processes, we performed additional simulations with a range of constant temperatures (0.5-25°C) to cover a wider range of climate conditions. So that the results could be evaluated separately for different combination of T_{GW} and Q scenarios.

2.3.3. *Aerobic zone delineation and NO_3^- removal fractions*

Based on simulated DO concentrations, we delimited the locations in each infiltrating flow path where groundwater DO≤2 mgL^{-1} (i.e., anaerobic conditions). In the following, we computed the convex envelope encompassing those points, which closely defines the aerobic zones (DO_z) around the stream for each simulated time-step by using the *boundary* function in MATLAB®. By doing so, we can assess the changes in the volume of the aerobic zone given the different Q and T_{GW} scenarios.

We quantified nitrate removal fractions (R_{NO3}) by calculating the cumulative amount of NO_3^- removed through denitrification in each flow path sub-section divided by the initial NO_3^- in each flow path:

$$R_{NO3} = \frac{denitrified\ NO3}{initial\ NO3} \tag{6}$$

The fraction ranges between 0 and 1, with larger values representing higher removal fractions, hence higher removal efficiency. A value of 1 represents complete removal of the initial flow path NO_3^-. This allowed us, for instance, to locate the time required to remove 50% of the initial NO_3^- concentration (R_{NO3}=0.5) in each scenario. We further computed the NO_3^- removal fractions on observation wells in the vicinity of the stream to assess how they change in the different scenarios. The results were compared to values calculated from field data as recently presented by Lutz *et al.* (2020). They computed NO_3^- removal fractions by combining end-member mixing and dual-isotope (analysis of N and O isotopes of NO_3^-) modelling to account for mixing of stream water and groundwater at the riparian wells of the study site.

3. Results

3.1. Hydrological modelling and validation

Autocalibrated parameter values were within the range of values reported in the literature, Table 1. Horizontal hydraulic conductivity anisotropies (between K_x and K_y) were obtained from the calibration, and ranged between 0.5 and 3.3, decreasing towards the top of the domain. The vertical hydraulic conductivity anisotropy (between K_{xy} and K_z) varied from 2.7 to 31 for the different model hydrogeological units (Figure 1b), and was the highest for the sandy units. Simulated groundwater hydraulic heads had an overall R^2=0.987 and RMSE=0.14 m, with an underestimation of heads towards the end of the simulation period (about 0.2 m on average, Figure 2a), which could affect v_{GW} to a certain extent. Individual R^2 for different wells ranged from 0.36 (near boundaries) to 0.96 (near the stream). NSE values for individual wells ranged from 0.2 to 0.81. Low values predominantly occurred in the downstream part of the domain (wells ML1-2 and ML5-2). Some gaps in groundwater data collection existed, which resulted in periods without high-frequency data due to probes malfunctioning. Simulated stream discharge matched the observed values and their seasonal dynamics (R^2=0.92 and NSE=0.85), Figure 2b.

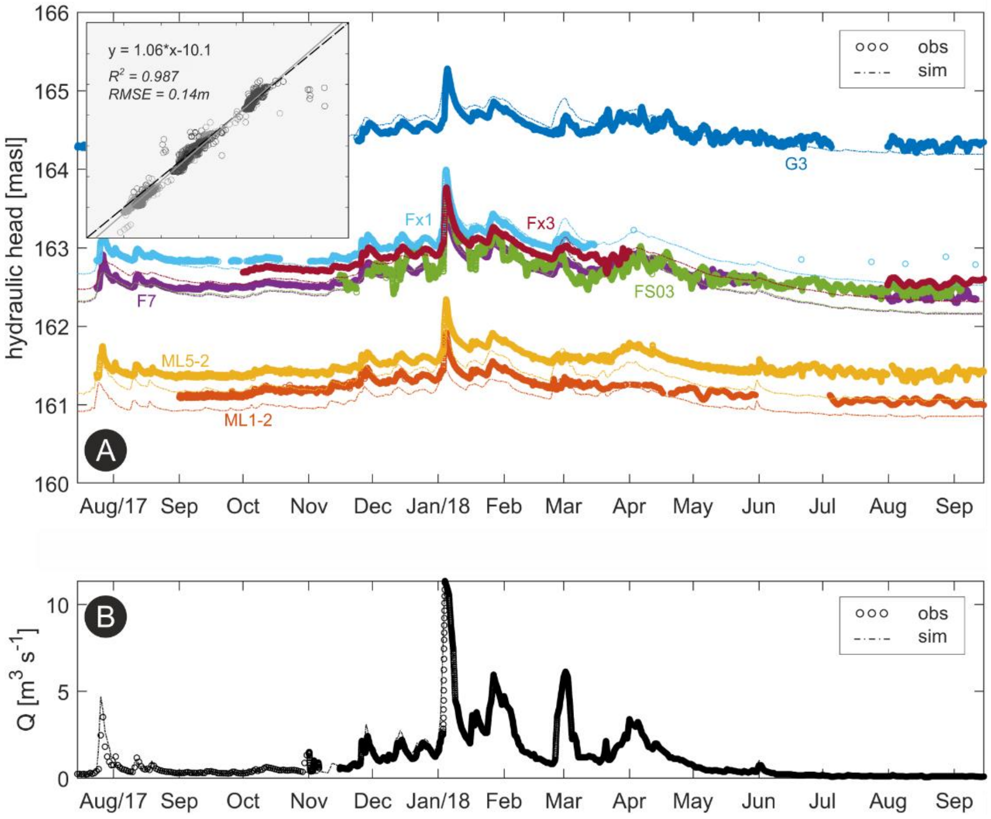

Figure 2: observed (circles) and simulated (dots) groundwater hydraulic heads **(a)** and stream discharge (Q) **(b)** for the simulated period. Different colours in (a) represent different observation wells. The inset plot in (a) shows the overall R^2 and RMSE between simulated and observed values.

Figure 3 presents the simulated tracer peak and mean transit-times from the tracer breakthrough curves. Simulations resulted in an overall R^2=0.51 between observed and simulated tracer peak-times, and R^2=0.74 between observed and simulated tracer mean transit-times. The simulations reasonably captured the general transit-time patterns despite the simplification of the geological media in the numerical model (Figure S7, supplementary material).

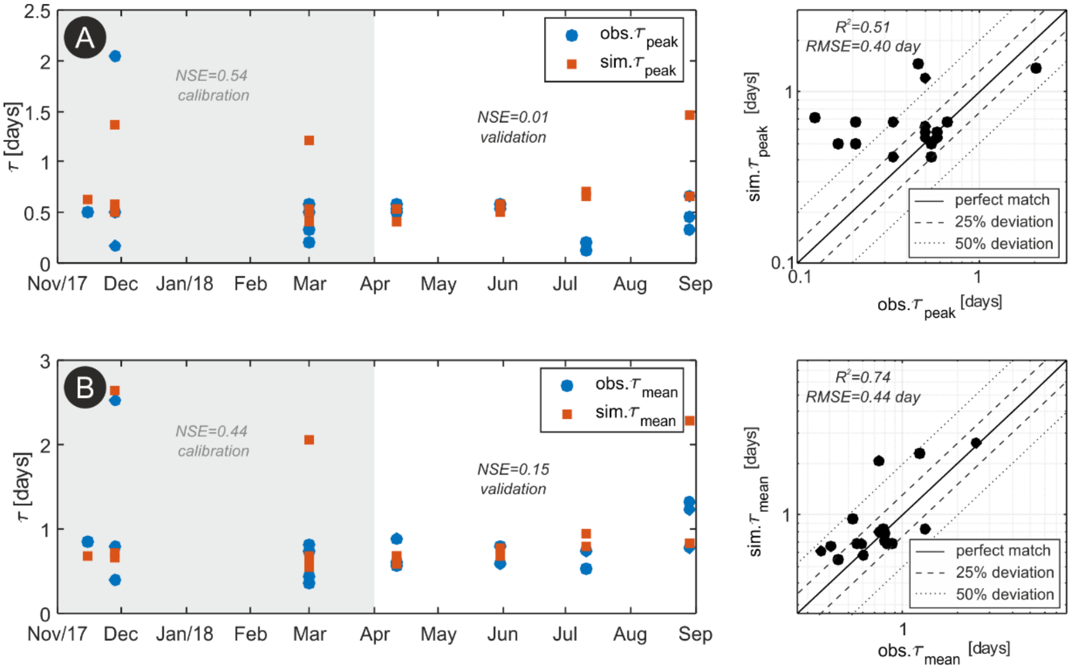

Figure 3: observed (blue circles) and simulated (orange squares) peak times **(a)** and mean transit-times **(b)** from tracer breakthrough curves. The grey shaded areas highlight the model calibration period. The *log-log* scatter plots on the right show the overall R^2 and RMSE between respective observed and simulated values.

3.2. Riparian particle tracking, surface water and groundwater exchange fluxes

Overall, groundwater velocity (v_{GW}) increased with increasing stream discharge (due to the increased hydraulic gradient between stream and riparian groundwater), and the calculated age of infiltrating SW particles decreased accordingly. The maximum age calculated for a particle before leaving the domain was 350 days, whereas average particles ages were 77 days and 20 days for low and high Q, respectively, see Figure 4. During high Q the SW infiltration flow paths diverge more from the stream in contrast to low Q, whereas particles reached deeper and further locations in the floodplain in comparison to low Q. Although most of the particles exited the domain through the subsurface downstream boundary, a few of them (around 1%) exfiltrated back into the stream (hyporheic flow paths). These hyporheic particles had transit-times around 2–4 days, and flow path lengths up to 50 m from infiltration to exfiltration point (Figure 5g-i and Figure S8, supplementary material).

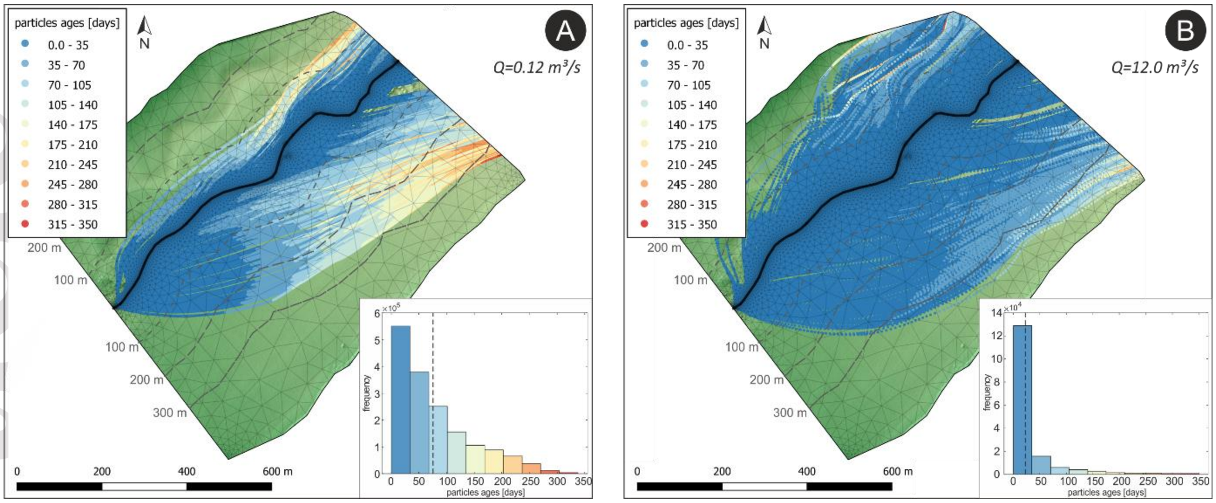

Figure 4: distribution of particles for low Q **(a)** and high Q **(b)** scenarios according to their age since infiltration. Dashed lines on maps highlight equal distances lines from the stream (100 m, 200 m, and 300 m). Dashed vertical lines in the inset histogram indicate the mean values of particle ages in each scenario (77 days and 20 days, respectively). Note: deeper flow paths are not visible in the plots.

Stream discharge variations that alter the hydraulic gradients between the stream and adjacent groundwater also regulated patterns and fluxes of SW-GW exchange. Three scenarios representing very low ($Q=0.12\ m^3s^{-1}$), average ($Q=1.44\ m^3s^{-1}$) and very high ($Q=12.0\ m^3s^{-1}$) stream discharge are shown in Figure 5 and depict the changes in SW-GW exchange fluxes and subsurface flow due to Q variations. The SW-GW exchange flux patterns revealed predominantly losing conditions for the overall reach. Small gaining regions developed only around a deep pool localised downstream of the simulated reach, Figure 5a-c. For the high Q scenario, the lengths of hyporheic flow paths and transit-times were the longest in comparison to lower Q scenarios (Figure 5g-i), which is opposite to what we observed for the losing flow paths leaving the domain at the downstream boundary (histograms in Figure 4). The spatial pattern of SW-GW exchange-flux (i.e., stream gaining and losing sections) and the simulated exchange volumes were consistent with field measurements (Schmadel et al., 2016), and within the range calculated from previous numerical models of subsections of the studied reach (Munz et al., 2017).

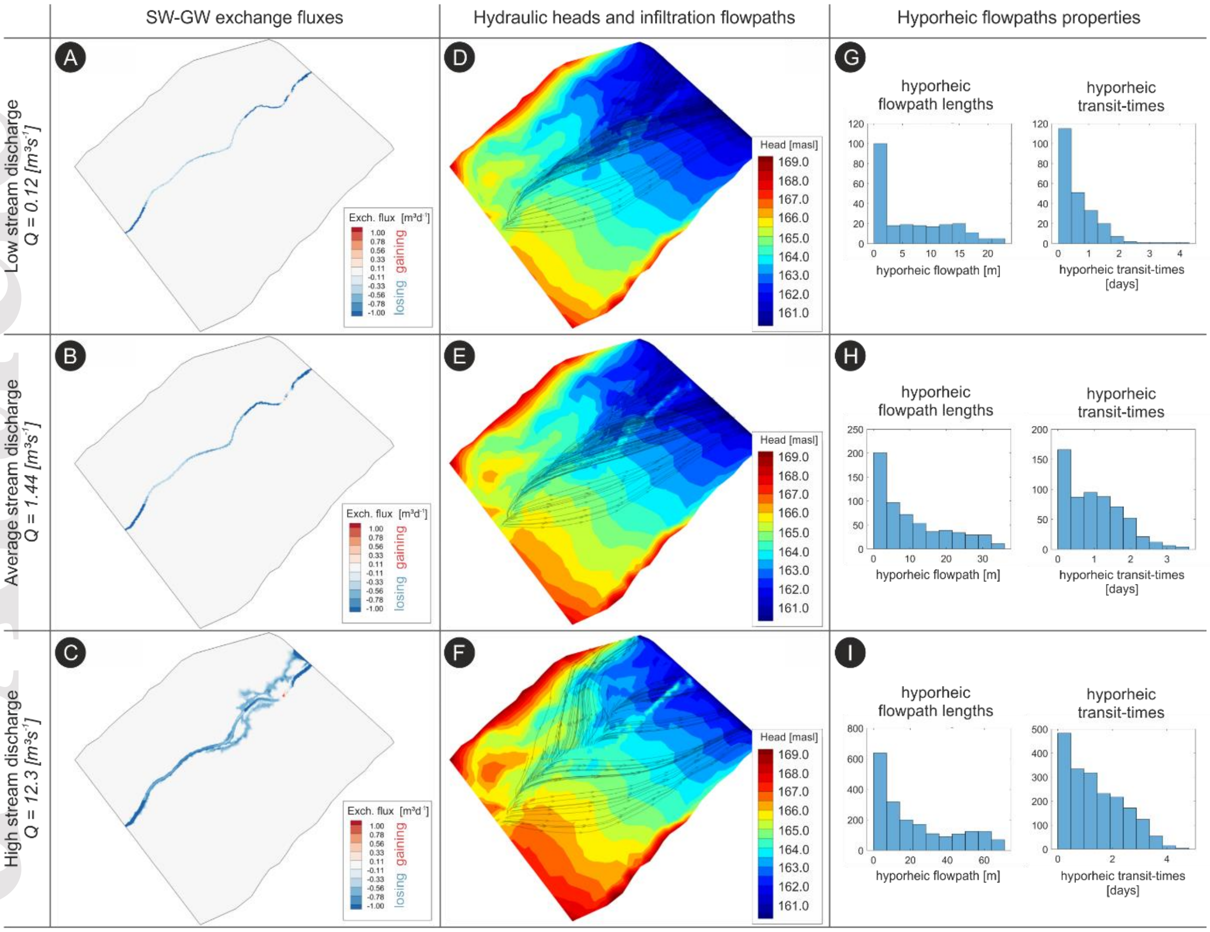

Figure 5: a-c) surface-water/groundwater exchange fluxes; **d-f)** hydraulic heads and subsurface flow paths of streambed particles; **g-i)** total lengths and transit-times of hyporheic flow paths.

3.3. Coupled reaction simulations

In this section we focus on the main results of DO and NO_3^- simulations with the flow path-reaction model based on the extracted particles from each time-step of the HGS model. Around 1,800 particles per time-step and their progressive transit through the domain (resulting in around 200,000 sub-sections per flow path) were coupled with the multispecies reaction simulation.

3.3.1. Riparian dissolved oxygen patterns

The simulated extent of the aerobic zone (DO_z), the volume with DO≥2.0 mgL^{-1} around the stream, is a function of the rate of advection of DO from the stream into the subsurface, the geometry of 3D flow field, and the rate of DO consumption (k_{DO}) in the riparian zone. Since infiltrating SW is DO-saturated (constant initial concentration throughout the simulations), DO_z volumes were mainly regulated by variations of k_{DO} which in turn was a function of temperature (Eq.(5)). Thus, warmer temperatures led to smaller DO_z, Figure 6. The DO_z volumes ranged between $5.0x10^4$–$3.1x10^5$ m^3 in summer and winter (winter DO_z up to 6 times greater than summer DO_z), respectively. High T_{GW} during summer associated with relatively longer infiltration transit-times (low Q), favour DO depletion within a small DO_z around the stream. Contrary, low T_{GW} in winter (which results in low k_{DO}) that is typically associated with shorter transit-times (high Q) led to an increasing extent of the DO_z, Figure 6b.

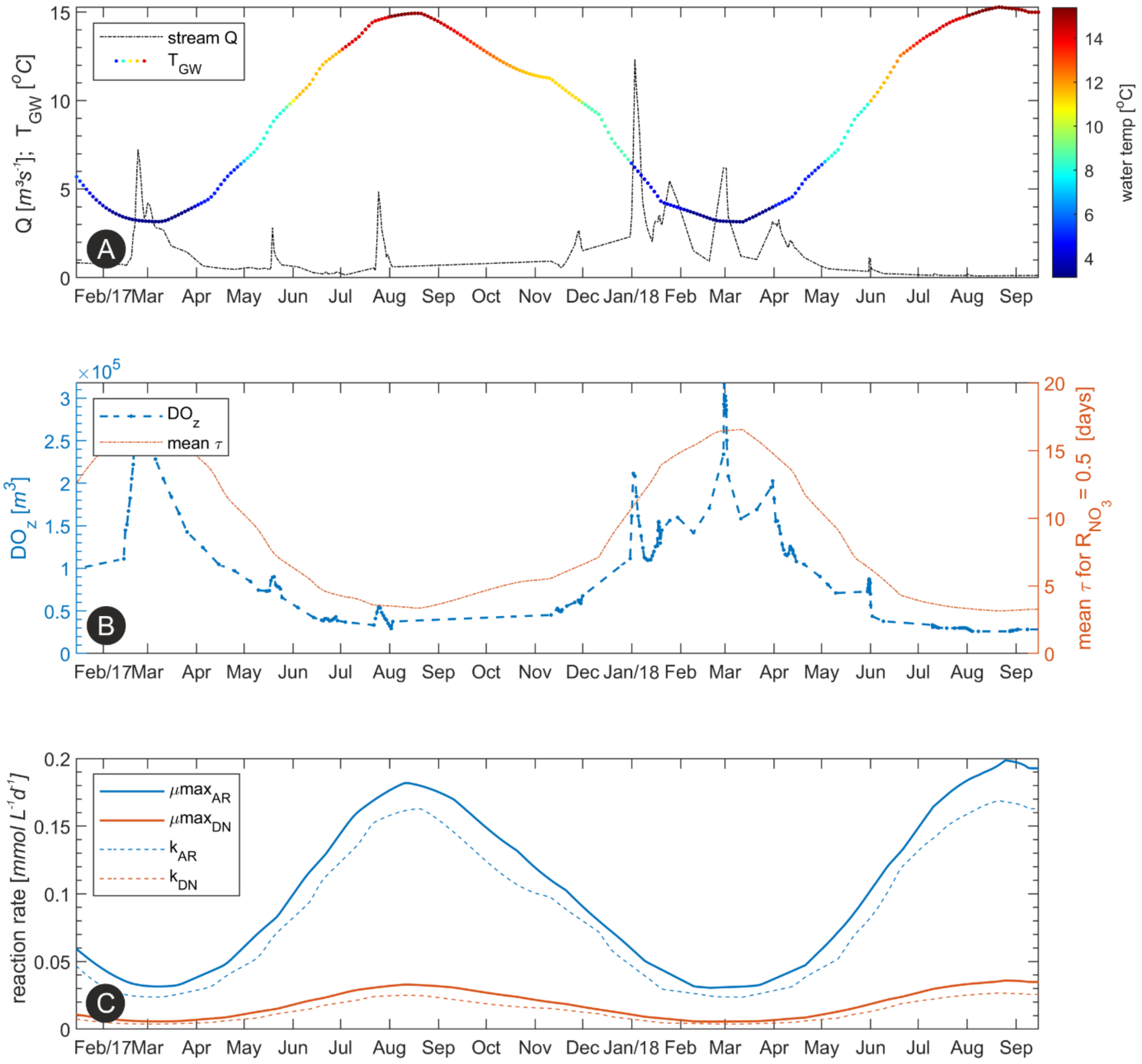

Figure 6: a) stream discharge (Q) and monthly groundwater temperature at the floodplain (T_{GW}); **(b)** computed aerobic zone volume (DO_Z) around the stream alongside mean transit-times for 50% removal of initial flow path nitrate (R_{NO3}=0.5); **(c)** maximum reaction rate coefficients for AR (μmax_{AR}) and DN (μmax_{DN}), and respective resulting rate coefficients (k_{AR}, k_{DN}) for the simulated period.

The effects of stream discharge only (and hence transit-time variations) on DO_z can be illustrated in the constant temperature simulations, Figure 7. For instance, under a constant low T_{GW} condition (T_{GW}=0.5 °C) the DO_z ranged between 5–15% ($2.5x10^5$–$7.0x10^5$ m³) of the total simulated domain for low (Q=0.12 m³ s^{-1}) and high stream discharge (Q=12.0 m³ s^{-1}), respectively, resulting in up to 200% increase in DO_z under high Q. On the other hand, under a constant high T_{GW} scenario (T_{GW}=25.0 °C) these values were fairly similar for both low and high Q, representing merely 0.2–0.4% ($0.7x10^4$–$2.0x10^4$ m³) of the floodplain, respectively, indicating the minor effect of transit-times variations with increasing T_{GW}.

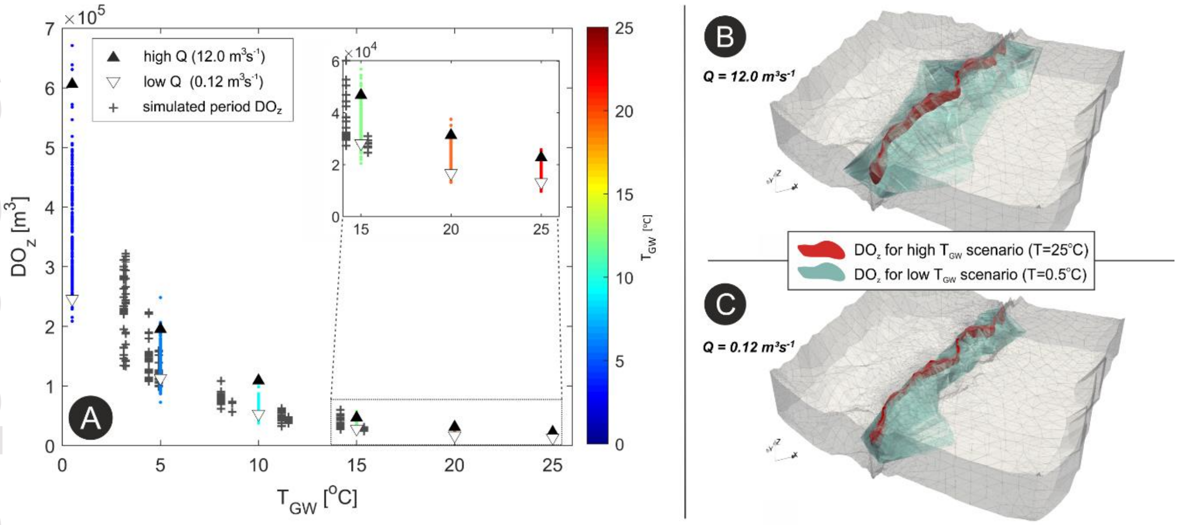

Figure 7: a) DO_z for different constant T_{GW} and varying Q scenarios. The black crosses denote the resulting DO_z volumes for the simulated period; **b-c)** 3D views of DO_z volumes for high **(b)** and for low **(c)** Q scenarios and two different T_{GW} values. Note the vertical exaggeration of the 3D plots (20x).

3.3.2. Denitrification and NO_3^- removal at the near stream riparian wells

Here we compare simulated and observed NO_3^- in terms of NO_3^- removal fractions (R_{NO3}) to simplify the interpretation of the two simulated scenarios (with varying and constant initial NO_3^- concentrations). By doing so, we can also disentangle the effects of varying initial NO_3^- concentrations from the effects of temperature and transit-time variations, and better evaluate the implications of overall elevated NO_3^- concentrations for floodplain reactivity. Results show that simulated R_{NO3} were similar regardless of the initial NO_3^- scenario, and were close to estimated R_{NO3} from observations in wells near the stream (Lutz et al., 2020), Figure 8a. The locations of wells are shown as black-crosses in Figure 9. The R_{NO3} are plotted against observed T_{GW} to enable a direct comparison to field-observed R_{NO3} values. Our R_{NO3} values were slightly larger for high temperature (R_{NO3}=0.7 vs. R_{NO3}=0.5), but the values show very similar ranges and relations with T_{GW}. R_{NO3} for the scenario with varying NO_3^- were slightly larger since the initial NO_3^- concentrations were generally lower than on the scenario with constant initial NO_3^-. For low T_{GW} conditions, denitrification (DN) is still supressed at these wells due to the presence of DO (DO_z expansion), shifting the location along the flow path where significant DN can take place further downstream. This also explains why resulting R_{NO3} were relatively similar regardless of the initial NO_3^- concentration scenario.

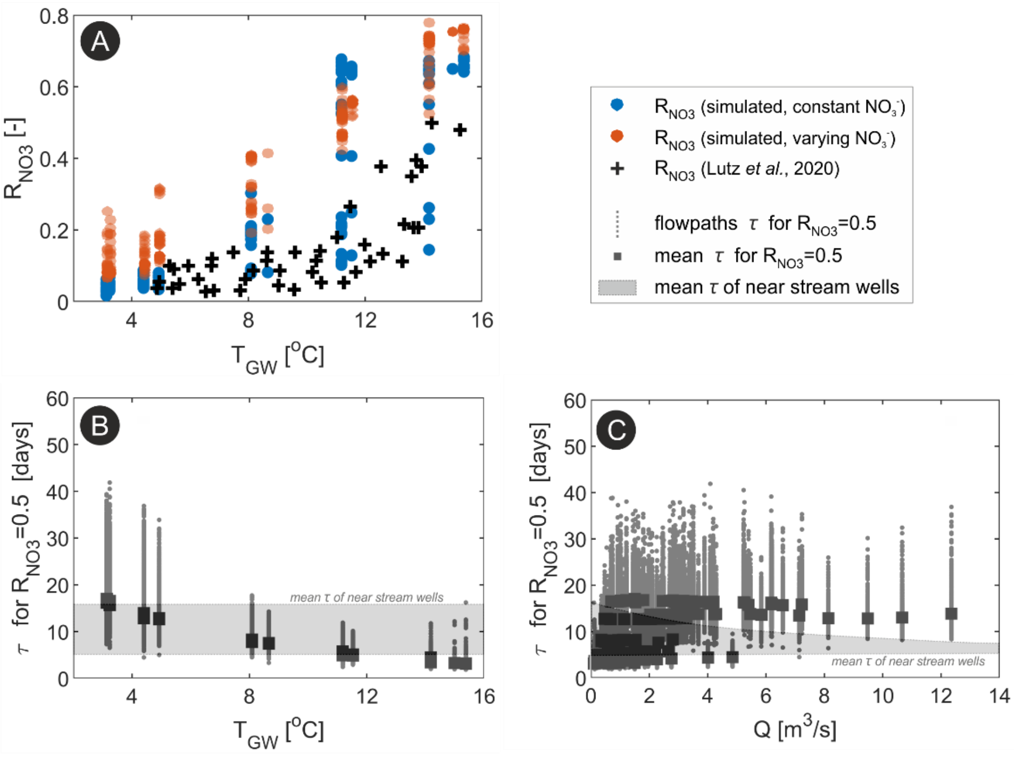

Figure 8: a) simulated NO_3^- removal fractions (R_{NO3}) on observation wells according to T_{GW} alongside R_{NO3} calculated by Lutz et al. (2020) (black crosses); time required for removing 50% of initial NO_3^- in each flow path and their mean values according to **(b)** T_{GW} and **(c)** Q for the simulation period.

Figure 8b-c shows the simulated transit-times required to achieve a removal fraction R_{NO3}=0.5 plotted versus T_{GW} and stream discharge (Q), alongside the mean τ for all wells over the simulation period. The time required for R_{NO3}=0.5 decreased from around 20 days (min=5 days, max=40 days) to about 5 days (min=2 days, max=15 days) with increasing T_{GW} (Figure 8b). In relation to Q, the time required for R_{NO3}=0.5 sharply increased from baseflow conditions up to Q=6 m³/s, and kept nearly constant for higher discharge values, Figure 8c. Results suggest that, based on computed mean τ for the observation wells, removal fractions of R_{NO3}=0.5 may or may not be realized depending on the hydrological and thermal conditions. For low Q values, R_{NO3} in this zone is at or slightly above 0.5, while for high Q a removal fraction of R_{NO3}=0.5 cannot be realised. This suggests that, the relatively low observed R_{NO3} in these wells for low T_{GW} conditions (and high stream discharge) does not indicate that generally no significant DN takes place along this infiltrating flow path, but rather that it will take place further downstream along this flow path.

3.3.3. Nitrate concentrations and denitrification patterns at the floodplain

The extent of the aerobic zone determines where other redox-sensitive reactions such as DN occur. Since high DN rates only occur after DO has been sufficiently depleted (i.e., near anaerobic conditions), as imposed by the inhibition factor in Eq.4, we observed that the computed mean τ required for R_{NO3}=0.5 increased with the volume of the DO_z (Figure 6b). Under a large DO_z, initial NO_3^- concentrations remain practically constant until considerable DN occurs at locations further away from the stream (after longer transit-times, Figure 8). As exemplified in Figure 9 for the simulations using constant T_{GW} values, significant DN only takes place at the fringes of the DO_z. As differences in the estimated removal fractions (R_{NO3}) between the two scenarios were minimal, we only show the results for simulations with constant initial NO_3^-. For the high T_{GW} scenario (25°C, Figure 9a-h), complete NO_3^- removal was reached closer to the stream (Figure 9b and 9f) mainly because of the high k_{DN} under warm conditions (up to 0.066 mmol $L^{-1}d^{-1}$ = 4 mg $L^{-1}d^{-1}$). At this condition, the DN fringe, the location where significant DN can take place is generally small, and only slightly larger under high Q conditions (Figure 9d and 9h), due to relatively small effects of transit-times variations under high temperature scenario (i.e., a more reaction controlled system).

Contrary, under very low-temperature conditions (0.5°C,Figure 9i-p) significant DN only occurred further away from the stream for both Q scenarios, given that aerobic conditions prevailed for most of the flow paths and DN was strongly inhibited, Figure 9i and 9m. In comparison to high T_{GW} scenarios, the DN fringe was larger since k_{DN} was generally smaller (only up to 1.9×10^{-3} mmol $L^{-1}d^{-1}$ = 0.12 mg $L^{-1}d^{-1}$) and longer times are required for removing the same amount of NO_3^-. The DN fringe was the largest for the combined high Q and low T_{GW} scenario, Figure 9p, however it was only slightly larger than the scenario of low Q and low T_{GW}, Figure 9L.

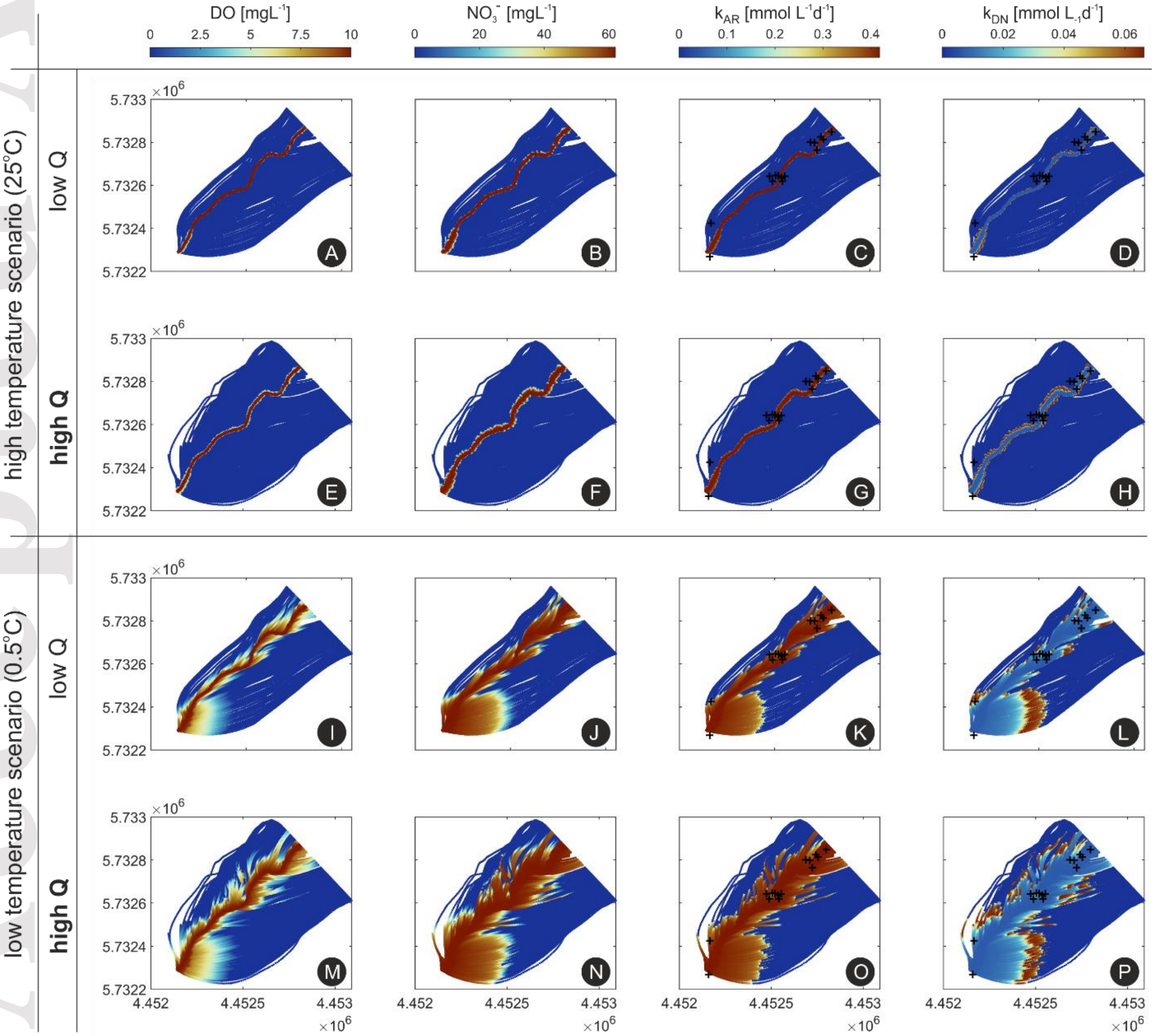

Figure 9: Distribution of dissolved oxygen (DO), Nitrate (NO_3^-), aerobic respiration (k_{AR}), and denitrification (k_{DN}) for four different scenarios of stream discharges and water temperature. The *low Q* and ***high Q*** represent 0.12 m^3s^{-1} and 12.0 m^3s^{-1}, respectively. The black crosses in the plots show the locations of the wells used for specific analyses of NO_3^- removal fractions. Note: deeper flow paths are not visible in the plots.

As the majority of simulated flow paths were long and most of the water did not immediately return to the stream via smaller hyporheic flow cells, DN and complete NO_3^- removal (R_{NO3}=1.0) still occurred at later times and further away from the stream (given that DOC was not completely consumed through AR). However, for the few hyporheic flow paths (infiltrating SW particles returning to the stream) observed in our model, maximum R_{NO3} values were only between 0.11 to 0.15 for low Q and high Q, respectively (for T_{GW}=25°C). The hyporheic R_{NO3} were slightly higher under high stream discharge due to somewhat longer hyporheic flow paths and transit-times in comparison to low discharge conditions (Figure S8, supplementary material).

3.3.4. Resulting effects on nitrate removal efficiency

Finally, to compare the combined effects of transit-times and temperature variations alongside the effects of varying NO_3^- on overall NO_3^- removal efficiency within the floodplain, we look on the resulting R_{NO3} of the different scenarios on the near stream observation wells. We also look specifically to the time required to achieve R_{NO3}=0.5, whereas shorter transit-times could be translated to higher removal efficiencies.

Generally, R_{NO3} at the near stream wells decreased with increasing discharge regardless of the considered T_{GW} scenario and the initial NO_3^- concentration (Figure 10a). Under high T_{GW}, overall high R_{NO3} are attained. It is important to note that, for the same T_{GW}, R_{NO3} values were slightly larger for low Q under the scenario with varying initial NO_3^- concentrations since for very low Q the initial NO_3^- at the beginning of the flow path was relatively smaller than the initial NO_3^- on the scenario with constant initial NO_3^- concentration.

From the scenario with constant initial NO_3^- concentrations (Figure 10b), we can depict the effects of transit-time and temperature variations on NO_3^- removal. First, the time required for R_{NO3}=0.5 strongly decreases with increasing T_{GW}, whereas only minor changes occur with stream discharge. Overall, the decrease in reactive efficiency (i.e., increase on the time required for R_{NO3}=0.5) is more prominent under low T_{GW} conditions indicating a more transport controlled system under such conditions. Under high T_{GW}, the time required for R_{NO3}=0.5 are generally shorter, whereas the effects due to stream discharge (hence transit-time variations) are minimal.

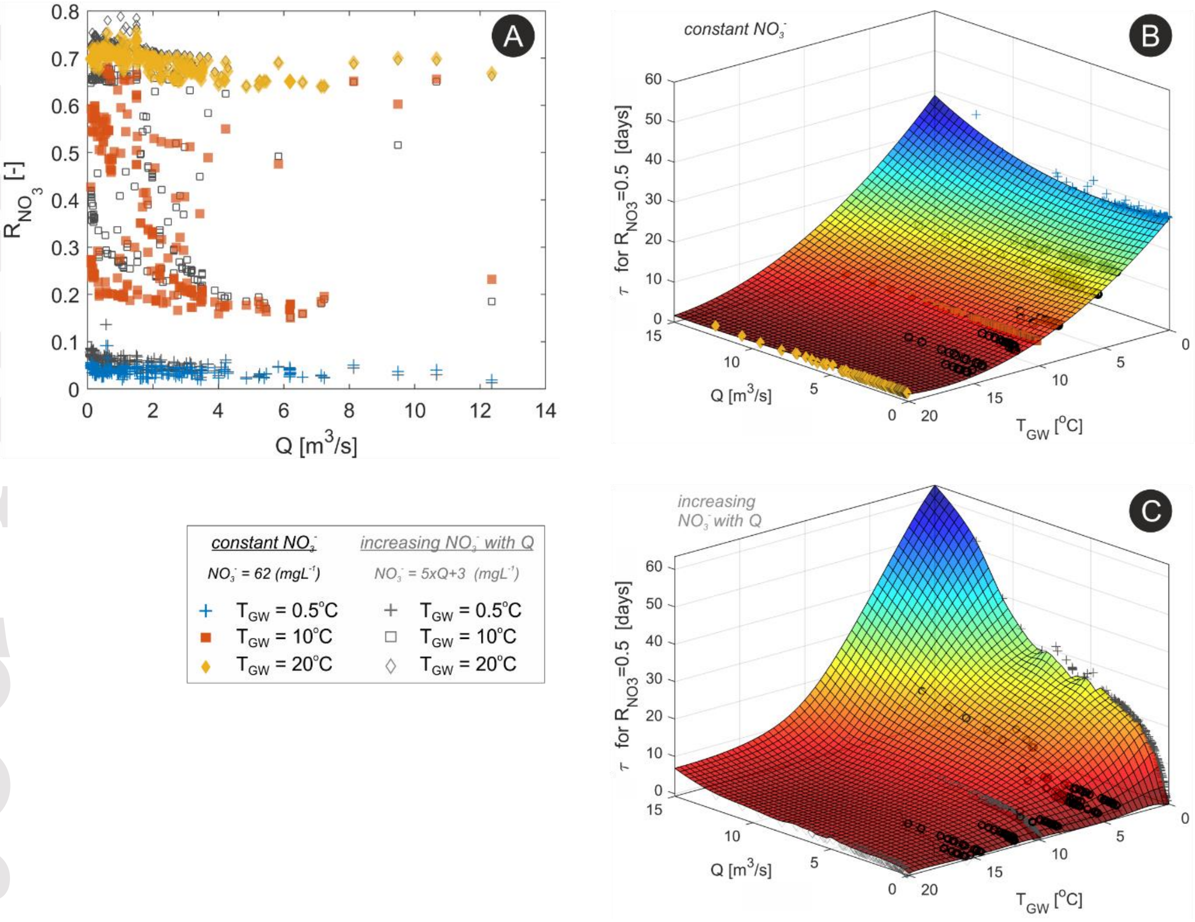

Figure 10: a) NO_3^- removal fractions (R_{NO3}) on the near stream wells versus Q for various T_{GW} and NO_3^- concentration scenarios; **(b)** mean transit-time required for R_{NO3}=0.5 for various Q and T_{GW} scenarios with constant initial NO_3^- concentrations; **(c)** mean transit-time required for R_{NO3}=0.5 for various Q and T_{GW} scenarios with varying initial NO_3^- concentrations; black circles in (a) and (b) show the results from the simulated period.

Results from the scenario of increasing initial NO_3^- concentration with Q show that, particularly under low T_{GW}, the time required for R_{NO3}=0.5 strongly increased with Q, from the nearly constant value of 35 days for the scenario with constant initial NO_3^- concentration to slightly more than 60 days. This emphasizes the effects of increasing solute concentration on the overall removal efficiency. In contrast, under high T_{GW}, the time required for R_{NO3}=0.5 only slightly increased with stream discharge (from 0.5 to 4 days). Compared to the constant initial NO_3^- concentration scenario, this minor absolute change under high T_{GW} indicates that the system is less sensitive to variations in solute concentrations and transit-times under high T_{GW}; in other words, a reaction controlled system. Again, for very low Q, the time required for R_{NO3}=0.5 under the scenario with varying initial NO_3^- concentrations were merely 0.5 day since the initial NO_3^- concentrations were relatively smaller than the initial NO_3^- on the scenario with constant initial NO_3^- concentration.

4. Discussion

In this study, integrated fluid flow and reactive solute transport considering temperature-dependent reaction rates, transient flow fields and stream discharge, as well as variations in instream solute concentrations at the scale of an entire stream corridor. To avoid the excessive computational costs of a fully coupled flow, heat transport and reactive solute transport model with temperature-dependent reaction rates at this scale, we intentionally employed a simpler flow path-reaction approach. This approach, which evaluates flow and reactive transport consecutively, was able to adequately reproduce general spatio-temporal patterns of redox-sensitive solute concentrations and removal fractions in the stream corridor, which were in line with previous estimates from field measurements (Lutz et al., 2020; Nogueira et al., 2021; Trauth et al., 2018). In our approach, once an integrated surface-subsurface flow model is calibrated, the extraction of flow paths, and the setup of the routine for temperature-dependent coupled reactions is straight forward, robust and fast. As such, the approach provides a convenient tool to evaluate observed biogeochemical patterns in groundwater in entire stream corridors and to explore the underlying dominant processes and reactions. For detailed assessments of complex local reactions and dynamics a fully coupled model might still be indispensable, but for a stream-corridor-scale assessment our approach provides a viable, computationally less demanding alternative. Limitations of our approach and recommendations for future improvements will be discussed further below.

4.1. Fully coupled 3D hydrological model

In this study, a transient 3D surface-subsurface flow model representing a 4th-order stream and its adjacent riparian aquifer was set up, aiming to avoid some of the limitations and possible pitfalls of common 2D steady-state simulations. Especially in near-stream areas where anisotropy of hydraulic conductivity and flow variability are high, transient simulations and an incorporation of multiple tracer-tests in the model calibration can yield more unbiased results and a more sound parameter calibration

(Gianni et al., 2019; Schilling et al., 2019; Xu & Gómez-Hernández, 2016). Hence, the incorporation of additional, less conventional field data, such as the results from field tracer-tests, in model calibration could be a viable alternative to more conventional calibration strategies in future studies of highly dynamic, coupled SW-GW systems.

The flow and transport parameters were in the range of expected values after calibration. Still, alluvial systems are typically characterised by a high degree of heterogeneity, and any numerical model can only include a simplified representation of the real subsurface structures. Despite that, the reasonable match between observed and simulated hydraulic heads and solute transport even in the highly dynamic near-stream zone suggests that fine-scale heterogeneities may only exert minor controls on general flow patterns and may have bearing mainly locally (Bardini et al., 2013). However, larger-scale patterns of exchange fluxes and hence also solute transport and reactions will be affected by larger-scale geologic heterogeneities (e.g. hydrofacies scale) at the scale of larger stream-corridors (Fleckenstein et al., 2006; Irvine et al., 2012; Pryshlak et al., 2015; Tang et al., 2015, 2017). Heterogeneities at this scale should generally be considered in future studies. A further assessment along those lines could be implemented by using transition probability-based geostatistical approaches to generate stochastic realizations of hydrofacies distributions (Fleckenstein et al., 2006; Labolle & Fogg, 2001), e.g. with software such as T-PROGS (Carle, 1999) and further calibrate hydrofacies properties using parameter estimation tools like PEST. On the other end, one could use pilot-points within the calibration process combined with Tikhonov regularisation, which allows a more constrained model parameterisation, while adding extra spatial flexibility for parameterising complex hydrogeological systems (John Doherty, 2003, 2015; Fienen et al., 2009; Moeck et al., 2015).

The calibrated model revealed predominantly losing conditions along almost the entire stream reach (on average 25% loss over a 1km reach, or 6000 m^3d^{-1} over a 1 km reach), which is comparable to previous field assessments at this site (Munz et al., 2017; Schmadel et al., 2016). The simulated flow paths, their extent, and associated transit-times are similar to those reported from other riparian zones and river-bank-filtration sites with similar systematically losing conditions (Liao et al., 2014; Munz et al., 2019; Poole et al., 2008; Su et al., 2007; Vogt, Hoehn, et al., 2010; Vogt, Schneider, et al., 2010). In our domain, most of the infiltrating SW does not return to the stream immediately within the modelled area, but based on flow continuity we expect its return at some point further downstream. Therefore turnover that takes place within the riparian aquifer even at larger distance from the stream, may eventually affect stream water quality further downstream.

4.2. Coupled reaction simulations and reactivity controls

One objective of this study was to simultaneously evaluate hydraulic and thermal effects on riparian solute turnover potentials. Our simulations revealed that the effect of transit-times on DO_z volumes diminishes with increasing T_{GW}, indicating that hydraulic and temperature effects should be evaluated jointly in stream corridors. Our simulations further indicated that in terms of denitrification, changes in stream discharge (and in turn subsurface transit-times) - under the assumption that concentrations do not change with stream discharge (e.g., pure hydraulic effects) - are of minor importance for NO_3^- removal fractions compared to changes in T_{GW}. Yet, the removal efficiency in the near stream wells was inversely related to stream discharge regardless of initial NO_3^- concentrations. Within the riparian zone, high v_{GW} under high discharge conditions and the resulting shorter transit-times from the point of infiltration to the observation wells led to smaller R_{NO3} values (Figure 10), even though extra solute influx increases reaction rate coefficients overall in the scenario of increasing NO_3^- concentrations with discharge. This is consistent with Sawyer (2015) and Shuai et al. (2017) who found that higher NO_3^- loads often resulted in lower removal efficiencies. For the scenario of increasing NO_3^- concentrations with discharge, the changes in overall R_{NO3} were especially large for low T_{GW} conditions indicating that the system becomes less sensitive to solute and transit-time variations with increasing T_{GW} and becomes increasingly reaction controlled. In terms of overall solute turnover, the effects of increasing temperature on reaction rates (i.e. the reaction-process) are faster and more prominent than the effects of increasing solute influx (i.e. solute-transport) in the simulations. This is supported by other studies, which demonstrated that solute removal fractions increase with the ratio between the time scale of solute-transport and the time-scale of the reaction-process expressed by the Damköhler number (Gu et al., 2007; Ocampo et al., 2006; Zarnetske et al., 2012). However, these studies did not account for the effects of variable temperatures.

In most of the hyporheic and in-stream studies assessing flow and biogeochemical processes, water temperature is usually set to a constant high value (e.g., 20°C) for simplicity, which in turn results in high reaction rate coefficients, with reaction processes being most constrained by the transit-time of water parcels through the subsurface. In contrast, Zheng et al. (2016) have shown the implications of different water temperature for biogeochemical processes occurring below the streambed. On top of their steady state simulations, our results revealed that the role of losing streams for denitrification at reach- and stream-corridor-scale might be overlooked, and nitrate removal efficiency might be underestimated (especially under low-temperature conditions) by investigations that are restricted to near-stream areas only. In other words, our results highlight that the longer infiltrating flow paths that deliver stream water into the more distant parts of the riparian aquifer in comparison to the rather short hyporheic flow paths allow for larger turnover rates and significant removal of nitrate even under low T_{GW} conditions.

The high DOC concentration of 20 mg L^{-1} in our simulations was intentionally chosen to avoid complete DOC exhaustion through AR, which would limit DN. This assumption, even though it could be considered unrealistic, reflects the general availability of electron donors also from other sources (e.g. particulate organic carbon in the sediments) and is supported by the good agreement between simulated and measured removal fractions (R_{NO3}) indicating that DOC is likely not a limiting factor for DN in the vicinity of the stream. The same assumption was already made by Trauth et al. (2018), who found R_{NO3} values between 0.15 and 0.75 similar to our simulated values (0.10-0.75). If we had considered only half of the initial 20 mg L^{-1} of DOC in SW (DOC= 10 mg L^{-1}), the new R_{NO3} at the observation wells would have been reduced by 40% (from 0.19 to 0.11 in average), whereas values were similar for low T_{GW} and differences were only observable for high T_{GW} (data not shown). Clearly, under such DOC limited conditions a complete NO_3^- removal is not expected to occur, however DN could still take place further away from the stream until bioavailable DOC (or any other electron donor) is fully depleted, leading to mean final R_{NO3} values between 0.3 and 0.4, for low and high T_{GW}, respectively (data not shown). Our results suggest that despite the low R_{NO3} in the vicinity of the stream during winter, significant NO_3^- removal is likely to take place at locations further into the floodplain aquifer. Unfortunately, no observations were available at those locations, which could have been used to directly validate our simulation results. Later NO_3^- removal would be solely limited by the flow path length (or total transit-time of the infiltrated water before returning to the stream), which could not be long enough for the system to reach anaerobic conditions for substantial denitrification to occur (as observed for the in-stream hyporheic flow paths). Alternatively, additional NO_3^- inputs would equally exhaust electron donors (such as DOC) and eventually inhibit heterotrophic denitrification (Rivett et al., 2008).

4.3. Limitations of this study and future work

The loose coupling of hydrology and biogeochemistry used in this work is an approach that can be easily transferred or adapted to other applications and, according to our evaluation based on field measurements, was able to capture main features and controlling factors of the hydro-biogeochemical system well. Nevertheless, with the flow path-reaction approach, hydrodynamic processes such as dispersion and diffusion that will affect solute concentrations within and between flow paths due to solute relocation are not taken into account. These processes would lead to more gradual and smooth anaerobic and DN fringes. However, we expect this effect to be greater only for low discharge conditions when a less advectively dominated system is expected, or under low T_{GW} when the system is generally more sensitive to changes in transport processes (i.e., transport limitation).

Moreover, infiltrating SW with different temperature from GW can affect subsurface reaction rate coefficients, which can be especially important within the first few meters around the streambed (Engelhardt et al., 2013; Munz et al., 2017; Nogueira et al., 2021; Song et al., 2018). But we claim that, due to strongly damped higher frequency heat signals from the stream, the reaction rate coefficients and the overall DO_z around the stream would not change to a great extent as they are mainly driven by the seasonal temperature variations (Figure S5, supplementary material). The HGS code can simulate heat fluxes, and the resulting transient temperature fields could be coupled with the reactions along flow paths in future work to assess the effects of event-driven heat fluxes for a more refined assessment of solute turnover in the SW-GW transition zone over different short-term and seasonal scales.

We did not carry out a detailed parameter sensitivity analysis on flow parameters and on solute simulations, as it was outside the scope of this study. Other hydrological and biogeochemical factors such as availability and ratio of nutrients, small scale sediment heterogeneity, and the actual relationship between DN rates and temperature, for instance, were not considered here but could impact NO_3^- removal fractions. Furthermore, there are no additional solute sources from the groundwater in our flow path reaction approach. This could be implemented to represent groundwater-borne solutes being gradually incorporated into the different flow path subsections according to other indicators such as particle locations in terms of distance from the stream and transit-times (e.g., mixing with groundwater, increasing NO_3^-). For instance, the presence of different carbon sources (e.g., decreasing DOC bioavailability) within alluvial aquifers is known to influence AR and DN rates differently than stream borne DOC (Shuai et al., 2017; Yvon-Durocher et al., 2012), and could be assessed in future studies. Equally, the presence of organic matter (OM) or other compounds within floodplain sediments could be considered to evaluate the contribution of different electron donors on denitrification as demonstrated by Pescimoro et al. (2019) for OM, and by Dwivedi et al. (2018) for reduced minerals at the aquifer material.

Finally, the presence of Ammonium (NH_4^+) in the infiltrating SW could also impact NO_3^- concentrations and denitrification. NH_4^+ would increase DO consumption through nitrification, and concomitant earlier NO_3^- production, leading to increased NO_3^- concentrations and ultimately increased k_{DN} depending on the $[NO_3^-]/[NH_4^+]$ ratios (Shuai et al., 2017; Zarnetske et al., 2011; Zheng et al., 2016). In our model, however, we neglected nitrification since locally NH_4^+ concentrations are very low (<0.1 mg L^{-1}) compared to stream and groundwater NO_3^- concentrations (Trauth et al., 2018) and therefore nitrate removal would prevail over production. Test simulations considering initial NH_4^+ concentrations of 0.2 mg L^{-1}, for instance, showed that the additional NO_3^- produced through nitrification would only amount to 1.0 mg L^{-1} in the observation wells near the stream (data not shown). If initial NH_4^+ concentrations were 10x higher (i.e., 2.0 mg L^{-1}), the additional NO_3^- would be between 0.6-6.0 mg L^{-1}. This and other relevant biogeochemical processes could be easily incorporated into the presented mechanistic modelling framework for future studies and at other sites where they might be more relevant.

5. Conclusions

Biogeochemical reactions in stream corridors are inherently complex due to the magnitude of factors affecting their occurrence and rates. Changes in flow dynamics controlling both water transit-time and the supply of reactants, seasonal water temperature changes, as well as the hydrogeological and streambed characteristics (like stream morphology, hydraulic properties) are some of the main factors contributing to the complex configuration of controls governing flow, transport and turnover. In this study, we presented a transient 3D fully-integrated surface-subsurface flow model of a riparian stream corridor, loosely coupled to a Lagrangian and temperature-dependent reactive transport model. We derived groundwater flow paths based on transient velocity fields and assessed how the interplay of the enumerated factors controls spatio-temporal patterns of riparian reactivity. The model was calibrated according to conventional and additional more unconventional observations (e.g., stream discharge and groundwater heads, and tracer-tests, respectively), which further reduced model uncertainties and could increase overall confidence in the robustness of the model for future applications. The presented modelling framework allowed flow and reactive transport simulations to be carried out in a highly efficient manner at the stream-corridor scale, lending results consistent to field observations, and can easily be employed in or adapted to other regions and conditions.

We found that while changes in transit-times driven by stream flow fluctuations affect DO and NO_3^- consumption rates, the effects are much smaller under high-temperature conditions than for low temperatures. The size of the aerobic zone around the stream controlled the occurrence of denitrification in the floodplain, inhibiting the process near the stream during low-temperature conditions due to persistently high DO concentrations. Furthermore, our results indicated that denitrification might still take place further away from the stream given sufficient availability of the reactants and that even under low-temperature conditions (and under limited DOC availability), up to 40% removal of initial NO_3^- can occur at later stages of transport along long infiltrating flow paths after DO has been sufficiently depleted. Despite the general decrease in NO_3^- removal fractions with increasing solute influx, removal efficiencies were more sensitive to changes in NO_3^- influx under low temperature than at high-temperature conditions.

There are multiple factors and feedbacks that control the complex removal efficiencies of NO_3^- in stream corridors. This work provides a tractable, practical approach to simulate relevant hydrological and biogeochemical process at a scale (stream corridor) relevant for management, while emphasizing the importance of considering the effects of both flow and temperature variations on solute turnover. Moreover, it highlights that studies restricted to the near stream area only (and rather short hyporheic flow paths) might disregard relevant processes that will ultimately affect overall system-scale turnover and water quality at downstream reaches, such as along infiltrating flow paths that travel long distances through the riparian aquifer before they may return to the stream. Our findings and the presented framework are generic and can be readily transferred to other sites for the assessment of reactive potential and flow dynamics in stream corridors.

6. Acknowledgments

GN performed the formal analysis, the investigation and wrote the original draft of the manuscript; all the authors contributed to review, final writing and editing; GN, CS, JF conceptualized the study; GN, CS, PB, DG and JF conceived the methodology; GN, CS, JF and DG worked on the validation of the study; CS and JF were responsible for supervision; JF was responsible for funding acquisition, resources and project administration. This research is part of the ENIGMA-ITN project that has received funding from the European Union's Horizon 2020 research and innovation programme under the Marie Sklodowska-Curie Grant Agreement No 722028. The field observational data, the numerical model files, as well as the flow path-reaction model script are publically available and can be assessed through: https://doi.org/10.4211/hs.476a188d9f894a77a3ed404949680cab.

7. References

Ahrens, J., Geveci, B., & Law, C. (2005). ParaView : An End-User Tool for Large-Data Visualization. In *Visualization Handbook* (pp. 717–731). Butterworh Beinemann. https://doi.org/https://doi.org/10.1016/B978-012387582-2/50038-1

Bardini, L., Boano, F., Cardenas, M. B., Sawyer, A. H., Revelli, R., & Ridolfi, L. (2013). Small-scale permeability heterogeneity has negligible effects on nutrient cycling in streambeds. *Geophysical Research Letters*, *40*(6), 1118–1122. https://doi.org/10.1002/grl.50224

Bernhardt, E. S., Blaszczak, J. R., Ficken, C. D., Fork, M. L., Kaiser, K. E., & Seybold, E. C. (2017). Control Points in Ecosystems: Moving Beyond the Hot Spot Hot Moment Concept. *Ecosystems*, *20*(4), 665–682. https://doi.org/10.1007/s10021-016-0103-y

Boano, F., Demaria, A., Revelli, R., & Ridolfi, L. (2010). Biogeochemical zonation due to intrameander hyporheic flow. *Water Resources Research*, *46*(2), 1–13. https://doi.org/10.1029/2008WR007583

Boulêtreau, S., Salvo, E., Lyautey, E., Mastrorillo, S., & Garabetian, F. (2012). Temperature dependence of denitrification in phototrophic river biofilms. *Science of the Total Environment*, *416*, 323–328. https://doi.org/10.1016/j.scitotenv.2011.11.066

Boutt, D. F., & Fleming, B. J. (2009). Implications of anthropogenic river stage fluctuations on mass transport in a valley fill aquifer. *Water Resources Research*, *45*(4), 1–14. https://doi.org/10.1029/2007WR006526

Briggs, M. A., Day-Lewis, F. D., Zarnetske, J. P., & Harvey, J. W. (2015). A physical explanation for the development of redox microzones in hyporheic flow. *Geophysical Research Letters*, *42*(11), 4402–4410. https://doi.org/10.1002/2015GL064200

Brunner, P., & Simmons, C. T. (2012). HydroGeoSphere: A Fully Integrated, Physically Based Hydrological Model. *Ground Water*, *50*(2), 170–176. https://doi.org/10.1111/j.1745-6584.2011.00882.x

Brunner, P., Simmons, C. T., & Cook, P. G. (2009). Spatial and temporal aspects of the transition from connection to disconnection between rivers, lakes and groundwater. *Journal of Hydrology*, *376*(1–2), 159–169. https://doi.org/10.1016/j.jhydrol.2009.07.023

Brunner, P., Therrien, R., Renard, P., Simmons, C. T., & Franssen, H. J. H. (2017). Advances in understanding river-groundwater interactions. *Reviews of Geophysics*, *55*(3), 818–854. https://doi.org/10.1002/2017RG000556

Čapek, P., Starke, R., Hofmockel, K. S., Bond-Lamberty, B., & Hess, N. (2019). Apparent temperature sensitivity of soil respiration can result from temperature driven changes in microbial biomass. *Soil Biology and Biochemistry*, *135*(February), 286–293. https://doi.org/10.1016/j.soilbio.2019.05.016

Carey, J. C., Tang, J., Templer, P. H., Kroeger, K. D., Crowther, T. W., Burton, A. J., et al. (2016). Temperature response of soil respiration largely unaltered with experimental warming. *Proceedings of the National Academy of Sciences of the United States of America*, *113*(48), 13797–13802. https://doi.org/10.1073/pnas.1605365113

Carle, S. F. (1999). *T-PROGS: Transition Probability Geostatistical Software, version 2.1*. *University of California, Davis*.

Chen, X., Chen, L., Stone, M. C., & Acharya, K. (2020). Assessing connectivity between the river channel and floodplains during high flows using hydrodynamic modeling and particle tracking analysis. *Journal of Hydrology*, *583*(July 2019), 124609. https://doi.org/10.1016/j.jhydrol.2020.124609

Diem, S., Cirpka, O. A., & Schirmer, M. (2013). Modeling the dynamics of oxygen consumption upon riverbank filtration by a stochastic–convective approach. *Journal of Hydrology*, *505*(November), 352–363. https://doi.org/10.1016/j.jhydrol.2013.10.015

Doherty, J. E., & Hunt, R. J. (2010). *Approaches to Highly Parameterized Inversion : A Guide to Using PEST for Groundwater-Model Calibration* (5169th ed.). U.S. Geological Survey Scientific Investigations Report.

Doherty, J. (1994). PEST: A Unique Computer Program for Model-independent Parameter Optimisation. *Water Down Under*, *94*, 551–554.

Doherty, J. (2018). PEST: Model-independent parameter estimation. User Manual. Australia: Watermark Numerical Computing.

Doherty, John. (2003). Ground water model calibration using pilot points and regularization. *Ground Water*. https://doi.org/10.1111/j.1745-6584.2003.tb02580.x

Doherty, John. (2015). *Calibration and Uncertainty Analysis for Complex Environmental Models*. *Groundwater*. https://doi.org/10.1111/gwat.12360

Dupas, R., Musolff, A., Jawitz, J. W., Rao, P. S. C., Jäger, C. G., Fleckenstein, J. H., et al. (2017). Carbon and nutrient export regimes from headwater catchments to downstream reaches. *Biogeosciences*, *14*(18), 4391–4407. https://doi.org/10.5194/bg-14-4391-2017

Dwivedi, D., Arora, B., Steefel, C. I., Dafflon, B., & Versteeg, R. (2018). Hot Spots and Hot Moments of Nitrogen in a Riparian Corridor. *Water Resources Research*, *54*(1), 205–222. https://doi.org/10.1002/2017WR022346

Ebel, B. A., Mirus, B. B., Heppner, C. S., VanderKwaak, J. E., & Loague, K. (2009). First-order exchange coefficient coupling for simulating surface water-groundwater interactions: parameter sensitivity and consistency with a physics-based approach. *Hydrological Processes*, *23*(13), 1949–1959. https://doi.org/10.1002/hyp.7279

Engelhardt, I., Prommer, H., Moore, C., Schulz, M., Schüth, C., & Ternes, T. A. (2013). Suitability of temperature, hydraulic heads, and acesulfame to quantify wastewater-related fluxes in the hyporheic and riparian zone. *Water Resources Research*, *49*(1), 426–440. https://doi.org/10.1029/2012WR012604

Fienen, M. N., Muffels, C. T., & Hunt, R. J. (2009). On constraining pilot point calibration with regularization in PEST. *Ground Water*, *47*(6), 835–844. https://doi.org/10.1111/j.1745-6584.2009.00579.x

Fleckenstein, J. H., Niswonger, R. G., & Fogg, G. E. (2006). River-aquifer interactions, geologic heterogeneity, and low-flow management. *Ground Water*, *44*(6), 837–852. https://doi.org/10.1111/j.1745-6584.2006.00190.x

Frei, S., Knorr, K. H., Peiffer, S., & Fleckenstein, J. H. (2012). Surface micro-topography causes hot spots of biogeochemical activity in wetland systems: A virtual modeling experiment. *Journal of Geophysical Research: Biogeosciences*, *117*(4), 1–18. https://doi.org/10.1029/2012JG002012

Genuchten, V. . M. (1980). A closed-form equation for predicting the hydraulic conductivity of unsaturated soils. *Soil Science Society of America Journal*, *44*(5), 892–898.

Gianni, G., Doherty, J., & Brunner, P. (2019). Conceptualization and Calibration of Anisotropic Alluvial Systems: Pitfalls and Biases. *Groundwater*, *57*(3), 409–419. https://doi.org/10.1111/gwat.12802

Greskowiak, J., Prommer, H., Massmann, G., & Nützmann, G. (2006). Modeling seasonal redox dynamics and the corresponding fate of the pharmaceutical residue phenazone during artificial recharge of groundwater. *Environmental Science and Technology*, *40*(21), 6615–6621. https://doi.org/10.1021/es052506t

Gu, C., Hornberger, G. M., Mills, A. L., Herman, J. S., & Flewelling, S. A. (2007). Nitrate reduction in streambed sediments: Effects of flow and biogeochemical kinetics. *Water Resources Research*, *43*(12). https://doi.org/10.1029/2007WR006027

Henzler, A. F., Greskowiak, J., & Massmann, G. (2016). Seasonality of temperatures and redox zonations during bank filtration - A modeling approach. *Journal of Hydrology*, *535*, 282–292. https://doi.org/10.1016/j.jhydrol.2016.01.044

Irvine, D. J., Brunner, P., Franssen, H.-J. H., & Simmons, C. T. (2012). Heterogeneous or homogeneous? Implications of simplifying heterogeneous streambeds in models of losing streams. *Journal of Hydrology*, *424–425*, 16–23. https://doi.org/10.1016/j.jhydrol.2011.11.051

Jasechko, S., Seybold, H., Perrone, D., Fan, Y., & Kirchner, J. W. (2021). Widespread potential loss of streamflow into underlying aquifers across the USA, *591*(July 2020). https://doi.org/10.1038/s41586-021-03311-x

Jensen, K. J., Engesgaard, P., Johnsen, A. R., Marti, V., & Nilsson, B. (2017). Hydrological mediated denitrification in groundwater below a seasonal flooded restored riparian zone. *Water Resources Research*, *53*(3), 2074–2094.

https://doi.org/10.1002/2016WR019581

Kirschbaum, M. U. F. (1995). The temperature dependence of soil organic matter decomposition, and the effect of global warming on soil organic C storage. *Soil Biology and Biochemistry*, *27*(6), 753–760. https://doi.org/10.1016/0038-0717(94)00242-S

Kirschbaum, M. U. F. (2000). Will changes in soil organic carbon act as a positive or negative feedback on global warming? *Biogeochemistry*, *48*(1), 21–51. https://doi.org/10.1023/A:1006238902976

Kurz, M. J., Drummond, J. D., Martí, E., Zarnetske, J. P., Lee-Cullin, J., Klaar, M. J., et al. (2017). Impacts of water level on metabolism and transient storage in vegetated lowland rivers: Insights from a mesocosm study. *Journal of Geophysical Research: Biogeosciences*, *122*(3), 628–644. https://doi.org/10.1002/2016JG003695

Labolle, E. M., & Fogg, G. E. (2001). Role of Molecular Diffusion in Contaminant Migration and Recovery in an Alluvial Aquifer System. *Transport in Porous Media*, *42*(1), 155–179. https://doi.org/10.1007/978-94-017-1278-1_8

Liang, X., Zhan, H., & Schilling, K. (2018). Spatiotemporal Responses of Groundwater Flow and Aquifer-River Exchanges to Flood Events. *Water Resources Research*, *54*(3), 1513–1532. https://doi.org/10.1002/2017WR022046

Liao, Z., Osenbrück, K., & Cirpka, O. A. (2014). Non-stationary nonparametric inference of river-to-groundwater travel-time distributions. *Journal of Hydrology*, *519*(PD), 3386–3399. https://doi.org/10.1016/j.jhydrol.2014.09.084

Liu, D., Zhao, J., Jeon, W. H., & Lee, J. Y. (2019). Solute dynamics across the stream-to-riparian continuum under different flood waves. *Hydrological Processes*, *33*(20), 2627–2641. https://doi.org/10.1002/hyp.13515

Lutz, S. R., Trauth, N., Musolff, A., Van Breukelen, B. M., Knöller, K., & Fleckenstein, J. H. (2020). How Important is Denitrification in Riparian Zones? Combining End-Member Mixing and Isotope Modeling to Quantify Nitrate Removal from Riparian Groundwater. *Water Resources Research*, *56*(1). https://doi.org/10.1029/2019WR025528

Maag, M., M. Malinovsky, and S. M. Nielsen (1997), Kinetics and temperature dependence of potential denitrification in riparian soils, J. Environ. Qual., 26, 215–223

Matsunaga, T., Karametaxas, G., von Gunten, H. R., & Lichtner, P. C. (1993). Redox chemistry of iron and manganese minerals in river-recharged aquifers: A model interpretation of a column experiment. Geochimica et Cosmochimica Acta, *57*(8), 1691–1704. https://doi.org/10.1016/0016-7037(93)90107-8Mayer, P. M., Reynolds, S. K., & Canfield, T. J. (2006). Riparian buffer width, vegetative cover, and nitrogen removal effectiveness: a review of current science and regulations. *Epa/600/R-05/118*, 1–40. Retrieved from http://nepis.epa.gov/Exe/ZyPDF.cgi/2000O182.PDF?Dockey=2000O182.PDF

Mayer, P. M., Reynolds, S. K., & Canfield, T. J. (2006). Riparian buffer width, vegetative cover, and nitrogen removal effectiveness: a review of current science and regulations. *Epa/600/R-05/118*, 1–40. Retrieved from http://nepis.epa.gov/Exe/ZyPDF.cgi/2000O182.PDF?Dockey=2000O182.PDF

Moeck, C., Hunkeler, D., & Brunner, P. (2015). Tutorials as a flexible alternative to GUIs: An example for advanced model calibration using Pilot Points. *Environmental Modelling & Software*, *66*(4), 78–86. https://doi.org/10.1016/j.envsoft.2014.12.018

Moore, C., Wöhling, T., & Doherty, J. (2010). Efficient regularization and uncertainty analysis using a global optimization methodology. *Water Resources Research*, *46*(8), 1–17. https://doi.org/10.1029/2009WR008627

Munz, M., Oswald, S. E., & Schmidt, C. (2017). Coupled Long-Term Simulation of Reach-Scale Water and Heat Fluxes Across the River-Groundwater Interface for Retrieving Hyporheic Residence Times and Temperature Dynamics. *Water Resources Research*, *53*(11), 8900–8924. https://doi.org/10.1002/2017WR020667

Munz, M., Oswald, S. E., Schäfferling, R., & Lensing, H.-J. (2019). Temperature-dependent redox zonation, nitrate removal and attenuation of organic micropollutants during bank filtration. *Water Research*, *162*(10), 225–235. https://doi.org/10.1016/j.watres.2019.06.041

Musolff, A., Schmidt, C., Selle, B., & Fleckenstein, J. H. (2015). Catchment controls on solute export. *Advances in Water Resources*, *86*(PA), 133–146. https://doi.org/10.1016/j.advwatres.2015.09.026

Nixdorf, E., & Trauth, N. (2018). Evaluating the reliability of time series analysis to estimate variable riparian travel times by numerical groundwater modelling. *Hydrological Processes*, *32*(3), 408–420. https://doi.org/10.1002/hyp.11428

Nogueira, G. E. H., Schmidt, C., Trauth, N., & Fleckenstein, J. H. (2021). Seasonal and short-term controls of riparian oxygen dynamics and the implications for redox processes. *Hydrological Processes*, *35*(2), 16. https://doi.org/10.1002/hyp.14055

O'Connell, A. M. (1990). Microbial decomposition (respiration) of litter in eucalypt forests of South-Western Australia: An empirical model based on laboratory incubations. *Soil Biology and Biochemistry*, *22*(2), 153–160. https://doi.org/10.1016/0038-0717(90)90080-J

Ocampo, C. J., Oldham, C. E., & Sivapalan, M. (2006). Nitrate attenuation in agricultural catchments: Shifting balances between transport and reaction. *Water Resources Research*, *42*(1), 1–16. https://doi.org/10.1029/2004WR003773

Oldham, C. E., Farrow, D. E., & Peiffer, S. (2013). A generalized Damköhler number for classifying material processing in hydrological systems. *Hydrology and Earth System Sciences*, *17*(3), 1133–1148. https://doi.org/10.5194/hess-17-1133-2013

Pescimoro, E., Boano, F., Sawyer, A. H., & Soltanian, M. R. (2019). Modeling Influence of Sediment Heterogeneity on Nutrient Cycling in Streambeds. *Water Resources Research*, *55*(5), 4082–4095. https://doi.org/10.1029/2018WR024221

Peterjohn, W. T. (1991). Denitrification: Enzyme content and activity in desert soils. *Soil Biology and Biochemistry*, *23*(9), 845–855. https://doi.org/10.1016/0038-0717(91)90096-3

Poole, G. C., O'Daniel, S. J., Jones, K. L., Woessner, W. W., Bernhardt, E. S., Helton, A. M., et al. (2008). Hydrologic spiralling: the role of multiple interactive flow paths in stream ecosystems. *River Research and Applications*, *24*(7), 1018–1031. https://doi.org/10.1002/rra.1099

Precht, E., Franke, U., Polerecky, L., & Huettel, M. (2004). Oxygen dynamics in permeable sediments with wave-driven pore water exchange. Limnology and Oceanography, 49(3), 693–705. https://doi.org/10.4319/lo.2004.49.3.0693

Pryshlak, T. T., Sawyer, A. H., Stonedahl, S. H., & Soltanian, M. R. (2015). Multiscale hyporheic exchange through strongly heterogeneous sediments. *Water Resources Research*, *51*(11), 9127–9140. https://doi.org/10.1002/2015WR017293

Rau, G. C., Andersen, M. S., McCallum, A. M., Roshan, H., & Acworth, R. I. (2014). Heat as a tracer to quantify water flow in near-surface sediments. *Earth-Science Reviews*, *129*, 40–58. https://doi.org/10.1016/j.earscirev.2013.10.015

Rivett, M. O., Buss, S. R., Morgan, P., Smith, J. W. N., & Bemment, C. D. (2008). Nitrate attenuation in groundwater: A review of biogeochemical controlling processes. *Water Research*, *42*(16), 4215–4232. https://doi.org/10.1016/j.watres.2008.07.020

Sawyer, A. H. (2015). Enhanced removal of groundwater-borne nitrate in heterogeneous aquatic sediments. *Geophysical Research Letters*, *42*(2), 403–410. https://doi.org/10.1002/2014GL062234

Sawyer, A. H., Kaplan, L. A., Lazareva, O., & Michael, H. A. (2014). Hydrologic dynamics and geochemical responses within a floodplain aquifer and hyporheic zone during Hurricane Sandy. *Water Resources Research*, *50*(6), 4877–4892. https://doi.org/10.1002/2013WR015101

Schilling, O. S., Cook, P. G., & Brunner, P. (2019). Beyond Classical Observations in Hydrogeology: The Advantages of Including Exchange Flux, Temperature, Tracer Concentration, Residence Time, and Soil Moisture

Observations in Groundwater Model Calibration. *Reviews of Geophysics*, *57*(1), 146–182. https://doi.org/10.1029/2018RG000619

Schipper, L. A., Hobbs, J. K., Rutledge, S., & Arcus, V. L. (2014). Thermodynamic theory explains the temperature optima of soil microbial processes and high Q10 values at low temperatures. *Global Change Biology*, *20*(11), 3578–3586. https://doi.org/10.1111/gcb.12596

Schmadel, N. M., Ward, A. S., Kurz, M. J., Fleckenstein, J. H., Zarnetske, J. P., Hannah, D. M., et al. (2016). Stream solute tracer timescales changing with discharge and reach length confound process interpretation. *Water Resources Research*, *52*(4), 3227–3245. https://doi.org/10.1002/2015WR018062

Sharma, L., Greskowiak, J., Ray, C., Eckert, P., & Prommer, H. (2012). Elucidating temperature effects on seasonal variations of biogeochemical turnover rates during riverbank filtration. *Journal of Hydrology*, *428–429*, 104–115. https://doi.org/10.1016/j.jhydrol.2012.01.028

Shuai, P., Cardenas, M. B., Knappett, P. S. K., Bennett, P. C., & Neilson, B. T. (2017). Denitrification in the banks of fluctuating rivers: The effects of river stage amplitude, sediment hydraulic conductivity and dispersivity, and ambient groundwater flow. *Water Resources Research*, *53*(9), 7951–7967. https://doi.org/10.1002/2017WR020610

Simmons, C. T., Brunner, P., Therrien, R., & Sudicky, E. A. (2020). Commemorating the 50th anniversary of the Freeze and Harlan (1969) Blueprint for a physically-based, digitally-simulated hydrologic response model. *Journal of Hydrology*, *584*(1969), 124309. https://doi.org/10.1016/j.jhydrol.2019.124309

Singh, T., Gomez-Velez, J. D., Wu, L., Wörman, A., Hannah, D. M., & Krause, S. (2020). Effects of Successive Peak Flow Events on Hyporheic Exchange and Residence Times. *Water Resources Research*, *56*(8). https://doi.org/10.1029/2020WR027113

Song, X., Chen, X., Stegen, J., Hammond, G., Song, H. S., Dai, H., et al. (2018). Drought Conditions Maximize the Impact of High-Frequency Flow Variations on Thermal Regimes and Biogeochemical Function in the Hyporheic Zone. *Water Resources Research*, *54*(10), 7361–7382. https://doi.org/10.1029/2018WR022586

Su, G. W., Jasperse, J., Seymour, D., Constantz, J., & Zhou, Q. (2007). Analysis of pumping-induced unsaturated regions beneath a perennial river. *Water Resources Research*, *43*(8), 1–14. https://doi.org/10.1029/2006WR005389

Tang, Q., Kurtz, W., Brunner, P., Vereecken, H., & Hendricks Franssen, H. J. (2015). Characterisation of river-aquifer exchange fluxes: The role of spatial patterns of riverbed hydraulic conductivities. *Journal of Hydrology*, *531*, 111–123. https://doi.org/10.1016/j.jhydrol.2015.08.019

Tang, Q., Kurtz, W., Schilling, O. S., Brunner, P., Vereecken, H., & Hendricks Franssen, H. J. (2017). The influence of riverbed heterogeneity patterns on river-aquifer exchange fluxes under different connection regimes. *Journal of Hydrology*, *554*, 383–396. https://doi.org/10.1016/j.jhydrol.2017.09.031

Therrien, R., McLaren, R. G., Sudicky, E. A., & Panday, S. M. (2010). HydroGeoSphere. A three-dimensional numerical model describing fully-integrated subsurface and surface flow and solute transport. *Groundwater Simulations Group*, 457. https://doi.org/10.5123/S1679-49742014000300002

Trauth, N., & Fleckenstein, J. H. (2017). Single discharge events increase reactive efficiency of the hyporheic zone. *Water Resources Research*, *53*(Jan), 779–798. https://doi.org/10.1111/j.1752-1688.1969.tb04897.x

Trauth, N., Musolff, A., Knöller, K., Kaden, U. S., Keller, T., Werban, U., & Fleckenstein, J. H. (2018). River water infiltration enhances denitrification efficiency in riparian groundwater. *Water Research*, *130*, 185–199. https://doi.org/10.1016/j.watres.2017.11.058

Trauth, N., Schmidt, C., Vieweg, M., Maier, U., & Fleckenstein, J. H. (2014). Hyporheic transport and biogeochemical reactions in pool-riffle systems under varying ambient groundwater flow conditions. *Journal of Geophysical Research: Biogeosciences*, *119*(5), 910–928. https://doi.org/10.1002/2013JG002586

Treese, S., Meixner, T., & Hogan, J. F. (2009). Clogging of an Effluent Dominated Semiarid River: A Conceptual Model of Stream-Aquifer Interactions. *JAWRA Journal of the American Water Resources Association*, *45*(4), 1047–1062. https://doi.org/10.1111/j.1752-1688.2009.00346.x

Veraart, A. J., de Klein, J. J. M., & Scheffer, M. (2011). Warming can boost denitrification disproportionately due to altered oxygen dynamics. *PLoS ONE*, *6*(3), 2–7. https://doi.org/10.1371/journal.pone.0018508

Vidon, P. G., & Hill, A. R. (2006). A landscape-based approach to estimate riparian hydrological and nitrate removal functions. *Journal of the American Water Resources Association*, *42*(4), 1099–1112. https://doi.org/10.1111/j.1752-1688.2006.tb04516.x

Vieweg, M., Kurz, M. J., Trauth, N., Fleckenstein, J. H., Musolff, A., & Schmidt, C. (2016). Estimating time-variable aerobic respiration in the streambed by combining electrical conductivity and dissolved oxygen time series. *Journal of Geophysical Research: Biogeosciences*, *121*(8), 2199–2215. https://doi.org/10.1002/2016JG003345

Vogt, T., Schneider, P., Hahn-Woernle, L., & Cirpka, O. A. (2010). Estimation of seepage rates in a losing stream by means of fiber-optic high-resolution vertical temperature profiling. *Journal of Hydrology*, *380*(1–2), 154–164. https://doi.org/10.1016/j.jhydrol.2009.10.033

Vogt, T., Hoehn, E., Schneider, P., Freund, A., Schirmer, M., & Cirpka, O. A. (2010). Fluctuations of electrical conductivity as a natural tracer for bank filtration in a losing stream. *Advances in Water Resources*, *33*(11), 1296–1308. https://doi.org/10.1016/j.advwatres.2010.02.007

Widdowson, M. A., Molz, F. J., & Benefield, L. D. (1988). A numerical transport model for oxygen- and nitrate-based respiration linked to substrate and nutrient availability in porous media. *Water Resources Research*, *24*(9), 1553–1565. https://doi.org/10.1029/WR024i009p01553

Wollschläger, U., Attinger, S., Borchardt, D., Brauns, M., Cuntz, M., Dietrich, P., et al. (2017). The Bode hydrological observatory: a platform for integrated, interdisciplinary hydro-ecological research within the TERENO Harz/Central German Lowland Observatory. *Environmental Earth Sciences*, *76*(1), 29. https://doi.org/10.1007/s12665-016-6327-5

Xu, T., & Gómez-Hernández, J. J. (2016). Characterization of non-Gaussian conductivities and porosities with hydraulic heads, solute concentrations, and water temperatures. *Water Resources Research*, *52*(8), 6111–6136. https://doi.org/10.1002/2016WR019011

Yvon-Durocher, G., Caffrey, J. M., Cescatti, A., Dossena, M., Giorgio, P. Del, Gasol, J. M., et al. (2012). Reconciling the temperature dependence of respiration across timescales and ecosystem types. *Nature*, *487*(7408), 472–476. https://doi.org/10.1038/nature11205

Zarnetske, J. P., Haggerty, R., Wondzell, S. M., & Baker, M. A. (2011). Dynamics of nitrate production and removal as a function of residence time in the hyporheic zone. *Journal of Geophysical Research: Biogeosciences*, *116*(1), 1–12. https://doi.org/10.1029/2010JG001356

Zarnetske, J. P., Haggerty, R., Wondzell, S. M., Bokil, V. A., & González-Pinzón, R. (2012). Coupled transport and reaction kinetics control the nitrate source-sink function of hyporheic zones. *Water Resources Research*, *48*(11), 1–15. https://doi.org/10.1029/2012WR011894

Zheng, L., Cardenas, M. B., & Wang, L. (2016). Temperature effects on nitrogen cycling and nitrate removal-production efficiency in bed form-induced hyporheic zones. *Journal of Geophysical Research G: Biogeosciences*, *121*(4), 1086–1103. https://doi.org/10.1002/2015JG003162